VIBRATIONAL POWER FLOW MEASUREMENT IN A BEAM USING ELECTRONIC SPECKLE PATTERN INTERFEROMETRY

SHORT TITLE: Power flow measurement using ESPI

T. Eck and S. J. Walsh

Department of Aeronautical and Automotive Engineering

Loughborough University, Loughborough, LE11 3TU. England

and

M. Dale and N. Taylor

Land Rover

Gaydon Test Centre, Warwick, CV35 0BL. England

23 Manuscript pages

23 Figures

2 Tables

This manuscript has not been submitted to any other journal.

ADDRESS FOR CORRESPONDENCE:

Dr. S. J. Walsh

Department of Aeronautical and Automotive Engineering

Loughborough University

Loughborough, LE11 3TU. UK

Telephone: +44 (0)1509 227 208

E-mail: S.J.Walsh@lboro.ac.uk

Summary

Vibrational power flow or structural intensity analysis is used to study the many paths of vibrational energy flow around complex flexible lightweight structures such as cars and aircraft. The vibrational power flow approach was developed so that the various paths of energy flow in the structure could be ranked in a rational way. A series of fundamental studies of power flow in simple structural elements, such as beams and plates, has been conducted over the last 25 years. These methods of measuring power flow have relied heavily on arrays of accelerometers mounted directly onto the structure. However, the practical application of power flow analysis has been limited by the lack of suitable measuring equipment. This paper reports on a preliminary case study which demonstrates the application of electronic speckle pattern interferometry (ESPI) also known as 'TV holography' to measure the vibrational power flow due to flexural vibrations in an experimental beam with anechoic terminations. Results obtained from the ESPI based measurements at three different frequencies are compared to conventional two-accelerometer power flow measurements and also to the measured power input to the structure. Although it is difficult to draw general conclusions about the ESPI based system from a single case study under ideal "infinite" beam conditions a number of observations about using the measurement system are summarised at the end of the paper.

PACS numbers:

43.40.-r Structural acoustics and vibration

1. Introduction

Vibrational power flow or structural intensity analysis is used to study the many paths of vibrational energy flow around complex flexible lightweight structures. For example, a flexible structure such as a car body when subjected to an excitation, or source of vibration, will transmit vibrational energy through the various parts of its structure. Eventually some of this energy will be radiated as unwanted noise often in areas remote from the source. The vibrational power transmission approach was developed so that the various paths of energy flow in the structure could be ranked in a rational way.

A series of fundamental studies of vibrational power flow in simple structural elements has been conducted over the last 25 years. Two notable contributions being by Noiseux in reference [1] and Pavic in reference [2]. However, the practical application of power flow analysis has been limited by the lack of suitable measuring equipment. Current methods of measuring power flow rely heavily upon arrays of accelerometers mounted directly onto the structure [3]. However, due to the practical limitation of using large arrays of accelerometers this method has severe drawbacks. For example [3], the vibrational power carried by bending waves in a plate can be expressed in terms of spatial derivatives of the normal (out of plane) vibrational velocity. To estimate the spatial derivatives using accelerometers finite difference approximations are introduced. For the complete formulation, 4 transducers are required for each power flow measurement location. However, the added mass of a large number of accelerometers may alter the dynamic characteristics of a lightweight structure. Further, noise contamination in the acquired data can lead to significant errors when estimating higher order spatial derivatives [4]. The method also requires a phase matching between transducer channels of less than 0.5˚. This is at the very limit of present accelerometer/charge amplifier technology.

Recent advances in laser technology have led to the development of non-contacting transducers capable of measuring the vibrational power or structural intensity of vibrating structures. In the simplest development laser vibrometers take point measurements of the structure

in a manner analogous to the current accelerometer technique [4]. However, this method does not overcome the errors associated with the finite difference approximation. Thus, an alternative wavenumber domain approach was suggested by Williams, Dardy and Fink in reference [5]. This method was applied analytically to a beam in flexure by Unglenieks and Bernard [6] and implemented experimentally using scanning laser vibrometers by Morikawa, Ueha and Nakamura [7]. However, the scanning vibrometer method is still cumbersome when mapping complex built-up structures.

A non-invasive technique that circumvents the limitations of the finite difference approximation is known as Nearfield Acoustic Holography (NAH) [8]. In this method the out-of-plane velocity of the structure is obtained by measuring the pressure field a fraction of a wavelength away from the surface of the structure. However, at frequencies much less than the critical frequency of the structure errors can be introduced in the reconstruction of the vibrational field from the acoustical pressure measurements. An alternative laser transducer system for vibrational power flow measurement is holographic interferometry. This method takes whole field measurements of the entire structure in a single instant [9]. Electronic Speckle Pattern Interferometry (ESPI), a development of holographic interferometry, uses a CCD video camera to capture this data every $^1/_{25}$th of a second, and is thus known as ‘TV holography’ [10]. However, conventional TV holography has the effect of averaging out the vibration phase information, thus, the resulting data represents the vibration amplitude field only. Both amplitude and phase are required for power flow analysis. Attempts to extend the method to enable measurement of the vibration phase are based upon stroboscopic illumination of the test structure. Recent developments by Jones et al. [11] and Towers et al. [12] use a stroboscopic phase stepping algorithm to accurately calculate a contiguous phase distribution of the vibrating surface.

The objective of this paper is to report on a preliminary case study which demonstrates the application of ESPI to measure the vibrational power flowing along an experimental ‘infinite’ beam structure at three different frequencies. In Section Two the definition of power flow in a beam is given along with equations to calculate the power flowing into and along a beam excited by a point

force. In Section Three the experimental beam apparatus is described and the equipment used for the measurement of the amplitude and phase of the flexural displacement is outlined. In Section Four the wavenumber technique used to calculate the power flow in the beam is explained. In Section Five the results of calculating the power flow along the beam from ESPI measurements are compared to measurements of the input power and to calculations of the power flow made using traditional accelerometer based measurements. The final section summarises the main findings of the case study. Of course, it is difficult to draw general conclusions about the accuracy of the ESPI power flow method from an investigation based upon the single case of a beam with anechoic terminations excited at a few selected frequencies. However, a number of observations are made regarding use of the ESPI based power flow system, in particular when compared to the conventional two-accelerometer measurement technique. Some suggestions for future study are also given.

2. Theory

2.1 Vibrational power flow in a beam

A derivation of vibrational power formulations based upon the forces and moments defined by classical Euler-Bernoulli theory for a beam in flexure is given in references [1,2]. The beam is considered to be lossless and is assumed to be homogeneous, isotropic and uniform. In terms of the complex vibrational displacement $u(x,t)$, the time-averaged power flow, P_x, which represents the power flowing along the beam in the x-direction is given in reference [6] as:

$$P_x = \frac{EI}{2}\Re\left(\frac{\partial^3 u}{\partial x^3}\cdot\left(\frac{\partial u}{\partial t}\right)^* - \frac{\partial^2 u}{\partial x^2}\cdot\left(\frac{\partial^2 u}{\partial x \partial t}\right)^*\right). \quad (1)$$

Here, *, denotes complex conjugate of the normal and angular velocities and, $\Re$, denotes the real part of the complex power flow. It can be seen in equation (1) that the product of half of the bending stiffness, $EI/2$, with spatial derivatives of the lateral out of plane displacement, $u(x,t)$ is

power flow propagating through a cross section of the beam. Thus, to determine the power flow in a beam spatial derivatives of the displacement have to be estimated.

2.2 Spatial derivative calculation

The traditional way of determining the spatial derivatives of the transverse displacement is to use a finite difference approximation [1,2]. An alternative approach, known as wavenumber technique, k-space method or Spatial Derivative technique, was proposed by Williams, Dardy and Fink [5] in 1985. This method utilises the spatial Fourier transform to evaluate the required spatial derivatives.

When using a temporal Fourier transform the acquired time signal is transformed into the frequency domain to detect its frequency components. Similarly, when using the spatial Fourier transform the acquired displacement signal is transformed into the wavenumber domain to detect its wavenumber spectrum. Mathematically, the forward and inverse spatial Fourier transforms are given, respectively, by

$$U(k) = FT\{u(x)\} = \int_{-\infty}^{\infty} u(x) \cdot e^{-jkx} dx, \tag{2}$$

$$u(x) = FT^{-1}\{U(k)\} = \frac{1}{2\pi} \int_{-\infty}^{\infty} U(k) \cdot e^{jkx} dk, \tag{3}$$

where, $u(x)$ is the spatial displacement, $U(k)$ is the wavenumber spectrum, FT denotes the forward Fourier transform and FT^{-1} denotes the inverse Fourier transform.

The spatial derivatives of the original signal are evaluated by multiplication of the wavenumber spectrum, $U(k)$, with the product of square root of minus one, j, and the respective wavenumber, k, of order n. This process can be expressed mathematically as:

$$\frac{\partial^n}{\partial x^n}[u(x)] = FT^{-1}\{(jk)^n \cdot FT[u(x)]\}, \tag{4}$$

The wavenumber domain signal is then transformed back into the spatial domain using the inverse spatial Fourier transform. Thus, to calculate the power flow in the beam given by equation (1), spatial derivatives of the displacement are evaluated and multiplied by their respective velocity

components. The real part is then extracted and multiplied by half the bending stiffness, $EI/2$, giving a time-averaged value for the power flow, P_x, along the beam.

2.3 Measurement of input power due to an applied force

One method of determining the power input to flexural waves in a beam by a transverse force is to use the theoretical value of point mobility of the equivalent infinite structure [13] given by

$$Y(\omega) = (1-i)\frac{1}{4 \cdot A \cdot \rho \cdot \sqrt{\omega}}\left(\frac{A\rho}{EI}\right)^{\frac{1}{4}}, \tag{5}$$

where, A is the cross-sectional area, and ρ the density of the beam. The input power is then simply the product of the input force power spectral density, G_{ff}, and the real part of the point mobility. Hence, the input power, $(P_{in})_{FP}$, is given by:

$$(P_{in})_{FP} = G_{ff} \cdot Re\{Y(\omega)\}. \tag{6}$$

For sinusoidal excitation this becomes

$$(P_{in})_{FP} = \frac{|F|^2}{2}\frac{1}{4 \cdot A \cdot \rho \cdot \sqrt{\omega}}\left(\frac{A\rho}{EI}\right)^{\frac{1}{4}}, \tag{7}$$

where, F is the amplitude of the harmonic force signal.

An alternative method to estimate the input power is to measure it directly using the imaginary part of cross-spectral density between the force and acceleration response at the excitation location. The input power, $(P_{in})_{FA}$, can be calculated by integrating the cross-spectral density between the force and response acceleration, G_{FA}, as follow:

$$(P_{in})_{FA} = \frac{1}{\omega} Im\{G_{FA}\}. \tag{8}$$

2.4 Accelerometer measurement of transmitted power

One technique to measure power flow in the far field of beam bending vibration uses a pair of accelerometers spaced between 0.15 and 0.2 of a wavelength [18]. The cross-spectral density

between the accelerometers, $G_{A2,A3}$, is measured and the power flow, P_{trans}, is calculated from the imaginary part using the following expression

$$P_{trans} = 2 \cdot \frac{\sqrt{\rho AEI}}{\Delta} \int_0^{\infty} \frac{Im\{G_{A2,A3}\}}{\omega^2} df \ , \tag{9}$$

where, Δ is the spacing between the two-accelerometers. If details of the test structure, such as the excitation frequency, and material and geometric properties, are known then a correction for the finite-difference approximation, can be applied [18]. Thus, the corrected power flow estimate, $(P_{trans})_{true}$, is

$$\left(P_{trans}\right)_{true} = P_{trans}\left(\frac{k\Delta}{sin(k\Delta)}\right), \tag{10}$$

where the correction factor is $k\Delta/\sin(k\Delta)$ and, k is the wavenumber.

2.5 Measurement of reflection coefficients

The reflection coefficient, R_1, for bending waves in the far field of the beam vibration is given by the ratio of reflected wave amplitude, A_r, to incident wave amplitude, A_i. Thus

$$R_1 = \frac{A_r}{A_i}. \tag{11}$$

An investigation of experimental methods to determine reflection coefficients in beams is given in reference [19]. For the research reported in this paper a relatively simple two-accelerometer technique appropriate for the vibrational far field is adopted. This has the advantage that the measurement of reflection coefficients can be made at the same time and using the same transducers as utilised for the two-accelerometer transmitted power measurements. Thus, an estimate of the reflection coefficient, R_2, is given by [19]

$$R_2 = \frac{H_{A2,A3} - e^{-jk\Delta}}{e^{jk\Delta} - H_{A2,A3}}, \tag{12}$$

where $H_{A2,A3}$ is the frequency response function calculated between accelerometer signals A_2 and A_3 using

$$H_{A2,A3} = \frac{G_{A2,A3}}{G_{A2,A2}}, \tag{13}$$

where $G_{A2,A2}$ is the autospectral density from accelerometer A_2.

3. Experimental Apparatus

3.1 Experimental “infinite” beam

The experiment was conducted on an “infinite” beam undergoing flexural motion. To simulate “infinite” wave propagation each end of a 6 m long, 60 mm by 10 mm cross-section, mild steel beam was embedded in a 1 m long box containing foam and sand to achieve an anechoic termination. The beam was suspended from a metal frame and the excitation point was in the middle of the beam as shown in Figure 1. ESPI measurements of vibration amplitude and phase were carried out in a region of the beam to the right of the excitation point at least 3/4 of a wavelength, λ, away from the excitation point or the anechoic termination. In the ESPI measurement region it was assumed that the near field wave component had already vanished and that only travelling waves existed.

To compare the ESPI power flow measurements with the traditional two-accelerometer technique, a pair of lightweight accelerometers were placed 51 mm apart within the ESPI measurement window as shown in Figure 1. The accelerometer spacing was chosen to be between 0.15 and 0.2 of a wavelength. The excitation force and point response were measured using a force transducer and accelerometer at the excitation location. All four channels were recorded on a multi-channel spectrum analyser.

3.2 ESPI measurement system

The ESPI measurement system is composed of a laser generation unit in combination with an optical head as shown in Figure 2. Conventional TV holography has the effect of integrating out the

phase information and, therefore, only the amplitude information is normally recorded. However, for power flow calculations the phase is also required. To measure the phase, a laser beam from a 150 mW continuous Frequency Doubled Nd:YAG laser was applied with a stroboscopic pulse that was synchronised with the excitation frequency of the structure. The optical modulator used to convert the continuous laser to stroboscopic pulses is known as Pockels cell. The Pockels cell, operating as a shutter, is located close to the laser generation unit as shown in Figure 2. From here an armoured fibre cable conducted the stroboscopic laser light to the optical, or interferometer, head. A directional coupler divided the laser beam into an object and a reference beam. In this device a piezo-electric crystal was used for phase modulation. The scattered object beam was focused by the SLR lens and produced interference fringes at the CCD camera lens interfering with the reference beam. The ESPI image was then recorded by a 512x512 low-light monochrome CCD camera with a 4:3 aspect ratio working with 25 frames per second. The dashed line in Figure 2 displays the components that are integrated into the optical, or interferometer head. The ESPI system was connected to a PC that triggered the Pockels cell with respect to the excitation frequency and was used to record the acquired image for post processing.

4. Method

A flow diagram of the power flow estimation method is shown in Figure 3. Stage 1 is to acquire the transverse displacement signal using the ESPI acquisition system described in Section 3. Also in Stage 1, the acquired ESPI data are manipulated in the spatial domain prior to Fourier transformation. The ESPI data window has a resolution of 512 by 512 pixels. From the beam displacement pattern lying within the ESPI data window a single row of pixels lying near the centre-line region of the beam was extracted. To satisfy the criterion for Fourier transform at least one cycle of the signal must be analysed. Further, to avoid problems of leakage associated with the rectangular window function, an integer number of waves must be used. Thus, as will be shown in

Section 5, a single cycle of the displacement wave data from the centre-line region of the beam was extracted.

The single cycle displacement data were transformed into the wavenumber domain by applying a spatial Fast Fourier transform (FFT) as shown in Stage 2. Thus, the wavenumber spectrum of the signal is calculated. Noise in the wavenumber spectrum will be amplified when calculating spatial derivatives because of the multiplication process. To diminish the effect of noise the use of an ideal k-space filtering process was also investigated. The ideal k-space filter was similar to those described in references [6, 14 and 15] and consisted of setting all amplitudes in the wavenumber spectrum equal to zero except for those wavenumbers corresponding to the excitation frequency. This procedure is indicated in Stage 3 of Figure 3. In Stage 4 spectral derivatives are calculated by multiplying the wavenumber spectrum, $U(k)$, with the square root of minus one, j, and the respective wavenumber k. This process is described mathematically by equation (4). The spatial derivatives of the signal are inverse Fourier transformed back into the spatial domain, shown within Stages 5 and 6. The final stage of the method, Stage 7, is to evaluate the time-averaged power flow in the beam by combining all the relevant signals to form equation (1).

5. Results

5.1 Experimental “infinite” beam

Figure 4(a) displays the modulus of the measured point mobility of the experimental beam over a frequency range of 10 Hz to 10,000 Hz. Also shown in Figure 4(a) is the theoretically determined driving point mobility of the equivalent infinite beam at the point of excitation. Taking into account the accelerometer spacing of Δ=51 mm, the beam’s material as well as geometrical properties, the excitation frequency has to be in the range of 800 Hz and 1430 Hz to minimise the effect of accelerometer phase mismatch [19]. For clarity reasons the frequency range of interest is enlarged, which can be seen in Figure 4(b). It can be seen in Figure 4 that the theoretical point mobility of the

equivalent infinite structure lies between the peaks and troughs of the measured data indicating, as expected, beam like behaviour of the test structure and also correctly assumed values for the material properties of the experimental beam. It is also apparent from the magnitude of the maxima and minima in the frequency spectra shown in Figure (4) that the anechoic terminations have a significant effect in reducing reflections from the boundaries of the experimental beam. Reflection coefficients for the beam measured at the specific ESPI excitation frequencies are discussed in Section 5.3.

5.2 ESPI displacement data

For the ESPI measurements the experimental beam as illustrated in Figure 1 was excited at three specific frequencies, 801 Hz, 1112 Hz and 1146 Hz, by the electro-dynamic exciter. As can be seen in Figure 4(b) these frequencies were selected as representing a local minima in the frequency response at 1112 Hz, a local maxima in the frequency response at 1146 Hz and a frequency close to the theoretical infinite beam response at 801 Hz. At each of these frequencies the amplitude and phase of the displacement within the ESPI data window were recorded.

In this work only the far field is considered, since the nearfield is almost vanished after a distance of approximately ¾ of the wavelength, λ, away from the excitation point. Thus, since wave motion within the ESPI window is assumed to be due to waves travelling in mutually opposite directions with amplitudes A_i and A_r, the complex beam displacement, $u(x,t)$, can be expressed as

$$u(x,t) = \left(A_r e^{jkx} + A_i e^{-jkx}\right)e^{j\omega t} = A\left[cos(\phi) - j \cdot sin(\phi)\right]e^{j\omega t}, \qquad (14)$$

where, A is the measured ESPI amplitude and, ϕ the measured ESPI phase. For ease of notation, equation (14) can be simplified by neglecting the harmonic temporal dependent term, $e^{j\omega t}$, since ESPI works at one particular frequency only and the image is time-averaged.

Figures 5, 6 and 7 show the measured ESPI amplitude and phase data at the excitation frequencies. The amplitude scale in Figure 5(a), Figure 6(a) and Figure 7(a) is shown in the bar on the right hand side and is given in meters and the phase scale in Figure 5(b), Figure 6(b) and Figure

7(b) is shown in radians in the range from $+\pi$ to $-\pi$. The *x*- and *z*-axis scales are given in terms of the number of data points recorded. As mentioned in Section 3 the CCD camera has a resolution of 512 by 512 points. The x-axis extends over the whole length of the ESPI data window from 0 to 512 data points. Since the beam width, 60 mm, was less than the height of the ESPI window and extended over approximately 50 rows, the z-axis is only shown from rows 120 to 190. The beam is shown lying between rows 129 and 179. It can be seen in Figure 5 that approximately two wavelengths of data have been recorded at 801 Hz. Similarly from Figure 6 and 7 it can be seen that approximately two and one half wavelengths of data have been recorded at 1112 Hz and 1146 Hz, respectively.

Figure 8 shows the same amplitude data as Figure 7 but with regions of high amplitude at the edges of the beam highlighted with circles. Thus, it can be seen in Figure 8 (here 1146 Hz) and to a lesser extent in Figures 5 and 6 that the amplitude as well as the phase is not constantly distributed across the beam width. This indicates an unwanted torsional vibration of the beam superimposed upon the lateral out of plane displacement and may have been due to the electro-dynamic exciter being located slightly away from the centre line of the beam. Clearly, for an idealised beam structure, such as this, the flexural and torsional vibrations should be uncoupled. However, any displacement in the beam due to torsional vibration will be interpreted by the ESPI power flow method as due to flexural waves, and, hence, corrupt the measured result.

Figures 9, 10 and 11 show three-dimensional plots as well as two-dimensional maps of the real part of the beam displacements generated by the recorded amplitude and phase, shown previously in Figures 5, 6 and 7. In all three figures it can be seen that the data in the x-direction beyond 400 points contains blank data regions because the ESPI measurement was not completely successful in recording the displacement at these locations. Unfortunately, this has the effect of reducing the useable range of data to less than two wavelengths at each excitation frequency. Further, to avoid problems of smearing and sidelobe leakage in the wavenumber domain it is desirable to use an integer number of wavelengths for Fourier analysis. Hence, a single cycle of displacement was extracted before transformation to the wavenumber domain. This was

accomplished by visually inspecting the displacement data in row 150, lying approximately along the centreline of the beam, and selecting the data between two successive peaks in the real part of the signal.

Figures 12, 13 and 14 show the single cycles of displacement data extracted from row 150 of the respective acquired ESPI data at each excitation frequency. Both, the real and imaginary parts of the signals are shown. In each case the real part is represented by a cosine type function and the imaginary part by a negative sine type function. However, it can be seen in Figures 12, 13 and 14 that the displacement data contain noise introduced by the optical ESPI measurement system. This optical noise will also be transformed into the wavenumber domain and, therefore, as shown in Section 5.3 will be filtered out prior to the spatial derivation process.

5.3 Wavenumber data

The extracted single cycle of each frequency were transformed into the wavenumber domain by applying the spatial Fourier transform. The spatial resolution, Δx, in the x-direction of the ESPI data acquisition process was $\Delta x = 1.7 \cdot 10^{-3}$ m, or 588 samples per meter. Thus, each cycle of extracted data contained approximately 200 data points. Hence, the wavenumber resolution, Δk, was approximately, $(588 \cdot 2\pi)/200 \approx 20$ radians/m. The resulting real parts of the wavenumber spectra of the respective frequencies are shown in Figures 15, 16 and 17. The wavenumber axis extends from -500 to +500 rad/m. It can be seen in Figures 15, 16 and 17 that there are components (spikes) at negative wavenumbers k=-18 rad/m, k=-21.7 rad/m and k=-22 rad/m, respectively, and components at positive wavenumbers k=18 rad/m, k=21.7 rad/m and k=22 rad/m, respectively. These wavenumbers correspond to the excitation frequencies of 801 Hz, 1112 Hz and 1146 Hz, respectively.

It can be seen in Figures 15, 16 and 17 that the negative wavenumber components are significantly larger than the respective positive components. This is to be expected as the negative wavenumber components represent waves travelling to the right through the ESPI window and the positive wavenumber components represent waves travelling to the left. Thus, the wave travelling

to the right is the incident wave propagating from the source and the wave travelling to the left is a wave reflected from the “anechoic” termination. The amplitudes of the right and left going waves shown in Figures 15, 16 and 17 are tabulated in Table 1. Also shown in Table 1 are the amplitudes of the reflection coefficients of the beam calculated directly from the wave amplitude data by using equation (11). As a comparison the amplitudes of the reflection coefficients calculated at each excitation frequency using the two-accelerometer method given by equation (12) are also tabulated in Table 1. It can be seen from inspection of the wave amplitudes and reflection coefficients tabulated in Table 1 that the amplitudes of the left going waves reflected from the anechoic termination are approximately one tenth of the amplitudes of the right going waves propagating directly from the electro-dynamic exciter. It can also be seen in Table 1 that the reflected wave component at 801 Hz is less than at the other two measurement frequencies. This pattern of behaviour is confirmed by the two-accelerometer calculation of reflection coefficients also shown in Table 1. It can be seen in Figures 15, 16 and 17 that there is also some low level noise in the wavenumber spectrum at wavenumbers not corresponding to the excitation frequency. This noise was removed with the ideal k-space filter mentioned in Section 4, before the spatial derivatives of the displacement were calculated.

5.4 Single-row power flow analysis

At each excitation frequency of the beam values of the input power and the transmitted power were calculated. These values are shown graphically in Figures 18, 19 and 20 and are tabulated in Table 2. Values of power input to the structure were estimated by applying equation (7) and also by applying equation (8). Because of the symmetrical nature of the experimental beam apparatus it was assumed that half the input power flowed away to the right and half away to the left of the electro-dynamic exciter. Therefore, the values for input power shown in Figures 18, 19 and 20 and tabulated in Table 2 are for the total input power divided by two. The values calculated using equation (7) are labelled ‘Input power $(P_{in})_{FP}$’ and those calculated using equation (8) are labelled ‘Input power $(P_{in})_{FA}$’. For comparison with the ESPI power flow data the input power values are

drawn as constants against distance along the ESPI window shown along the x-axis in Figures 18, 19 and 20. It can be seen in Figures 18, 19 and 20 that at each excitation frequency the values of input power calculated using equation (7) differ from the corresponding values calculated using equation (8). It is assumed that the measurements of input power based upon equation (8), which uses the cross-spectral density between the applied force and the resulting point response are more accurate than those obtained using equation (7) which relies upon a theoretical value of the equivalent infinite structure. This may explain the discrepancies between the values of 'Input power $(P_{in})_{FP}$' and 'Input power $(P_{in})_{FA}$' shown in Figures 18, 19 and 20. For example, it was shown in Figure 4 that the point mobility of the experimental beam followed the trend of the equivalent infinite beam but did not match it at all excitation frequencies. Hence, any measurement of input power based upon using the theoretical value of the infinite beam response may differ from the actual power input to the structure. However, the values of input power calculated using the infinite beam response, $(P_{in})_{FP}$, are retained in the following analysis as they act as a secondary check on the data.

Values of the transmitted power calculated using the traditional two acceleration technique described in Section 2 are also shown in Figures 18, 19 and 20 and tabulated in Table 2. The values of transmitted power calculated using equation (9) are labelled 'Transmitted power P_{trans}'. Similarly, the values of transmitted power calculated using equation (10) are labelled 'Corrected transmitted power $(P_{trans})_{true}$'. As these measurements were made at a single location on the beam they are drawn as constants against distance along the x-axis in Figures 18, 19 and 20. It can be seen in Figures 18, 19 and 20 that the corrected values for transmitted power, $(P_{trans})_{true}$, lie closer to the cross-spectral density measurements of input power, $(P_{in})_{FA}$, than the non-corrected values of transmitted power, P_{trans}, except for the 1112 Hz measurement. Since the values of corrected transmitted power, $(P_{trans})_{true}$, are not biased by the finite difference approximation they are assumed to give a more accurate estimation of the transmitted power than the non-corrected values of transmitted power, P_{trans}. Although in practical situations prior knowledge of the beam's

excitation frequency and material and geometric properties, which enable the finite difference correction to be made, may not be available.

As noted earlier, row 150 of the ESPI data coincided approximately with the centre-line of the beam. Hence, this single row was selected for ESPI power flow analysis. Thus, at each position along row 150 the vibrational power flow was calculated using equation (1). Figures 18, 19 and 20 show the ESPI calculated power flow due to the propagating, right going, waves against distance in meters along the section of beam inside the ESPI window. The power flow calculated without using the ideal k-space filter is labelled as 'Raw ESPI power $(P_x)_{raw}$'. Similarly, the power flow calculated by applying the ideal k-space filter is labelled as 'Filtered ESPI power $(P_x)_{filtered}$'. Figures 18, 19 and 20 indicate that the ESPI calculated power flow varies with distance along the beam. This was not expected, as the energy flow should be constant along the length of the beam. However, this erroneous variation in power flow may be due to the effect of the torsional vibration identified earlier or noise on the acquired ESPI data. It can also be seen in Figure 18, 19 and 20 that the filtered ESPI power flow values, $(P_x)_{filtered}$, exhibit less variability with distance along the beam than the corresponding values for the non-filtered ESPI power flow values, $(P_x)_{raw}$'. Hence the k-space filtering operation appears to have smoothed the estimation of ESPI power flow. It should also be noted that because of the size of the ESPI window only one wavelength of the displacement was used for the ESPI power flow calculation. Increasing the size of the ESPI window to include more wavelengths will improve the resolution in the wavenumber domain and, therefore, would be expected to provide a more accurate estimation of the power flow.

A summary of the various power quantities, obtained by analysing row 150, is tabulated in Table 2. The transmitted power values derived from the ESPI measurement data were formed by taking an average of all the calculated values of transmitted power along row 150. One advantage of wavenumber domain processing over the traditional accelerometer based power flow techniques is that the vibrational power associated with left and right going waves can be identified. Hence, the transmitted power due to the waves reflected from the anechoic termination and, thus, travelling to the left are also listed in Table 2. It can be seen in Table 2 that the filtered ESPI transmitted power

values due to the reflected waves travelling to the left are significantly less than the corresponding power values due to the respective propagating waves going to the right. This corresponds to the observation made about the wavenumber spectrum in Section 5.3, where it was noted that the propagating wave amplitudes were approximately ten times the amplitude of the respective reflected wave amplitudes. Since the power in a signal is related to the square of its amplitude it can be expected that the transmitted power due to the reflected waves will be approximately 1% of the transmitted power due to the respective propagating waves.

5.5 Multi-row power flow analysis

It was shown in Figures 5-8 that to varying degrees at each measurement frequency, unwanted torsional vibration was superimposed upon the flexural beam vibration. Potentially this will affect the measured ESPI power flow results. In the previous section, row 150, lying in the centre-line region of the beam, was selected in order to minimise the influence of torsion upon the measured results. However, as an alternative an average value of the power flow can be formed by using a multi-row analysis. For this approach, the previously described power flow procedure, by means of ESPI data acquisition, single cycle extraction, ideal filtering procedure as well as determination of the power flow was carried out for each useable row of ESPI data across the beam width.

Figures 21, 22 and Figure 23 show the result of the multi-row analysis of all three excitation frequencies for both the right and left going waves. The distribution of the power flow is shown versus the ESPI displacement row number across the beam width and the dashed line displays an average formed from all the single-row power flow data. It would appear from Figures 21, 22 and 23 that the power flow along the beam varies with each row across the beam width. This should not be the case for pure bending waves in a straight beam. Thus, Figures 21, 22 and 23 indicate that the ESPI power flow technique is sensitive to the actual row selected for analysis. Therefore, an average value of the ESPI power flow formed from a multi-row analysis should be more representative of the actual transmitted power flow along the beam than the values calculated from

a single row, such as row 150. Thus, the average values of ESPI power flow calculated from the multi-row analysis are also tabulated in Table 2.

A comparison can now be made between the power transmitted along the beam calculated using the two-accelerometer method and the multi-row filtered ESPI power flow technique. It is assumed that the values of half the input power calculated using the cross-spectral density method, $(P_{in})_{FA}$, provide the best estimates, or reference values, for power flow to the right of the electro-dynamic exciter. It can be seen from inspection of the values tabulated in Table 2 that the corrected accelerometer technique produced the best estimate of power flow along the beam at all three excitation frequencies. It can also be seen from inspection of the values in Table 2 that at 801 Hz and 1112 Hz the filtered ESPI multi-row net power technique produced better estimates than the non-corrected accelerometer method. However, at 1146 Hz the non-corrected accelerometer value, P_{trans}, gave a better estimate than the corresponding filtered ESPI net power flow value, $(P_x)_{filtered\text{-}net\text{-}multi}$. This may be due to the greater sensitivity of the ESPI method to unwanted torsional vibration or to the effect of higher amplitude reflected waves at this frequency.

6. Summary

This paper has reported on a preliminary case study which has demonstrated the application of ESPI to measure the vibrational power flow in a straight beam with anechoic terminations. The experimental “infinite” beam apparatus was excited at three different frequencies by an harmonic force and the power flow due to flexural waves was measured in the vibrational far field away from the source of excitation and the anechoic terminations. Measurements made using the ESPI based power flow method were compared to measurements made using the traditional two-accelerometer technique as well as to measurements of the power input to the structure. Of course, it is difficult to draw general conclusions about the accuracy of the ESPI power flow system from a single case study based on ideal “infinite” beam conditions. However, a number of observations were made when using the ESPI based power flow method and there are summarised below:

1. The ESPI power flow technique was more time consuming to apply than the two-accelerometer method as individual cycles of data need to be extracted manually from the ESPI data.
2. The wavenumber domain resolution and, hence, accuracy of the ESPI power flow technique was limited by the number of complete wavelengths of displacement available for analysis in the vibrational far field.
3. Noise in the wavenumber spectrum was amplified when calculating spatial derivatives because of the multiplication process. More accurate estimates of the power flow were obtained if this noise was filtered out prior to the ESPI power flow calculation.
4. The ESPI technique was sensitive to the row location across the beam width selected for analysis. Therefore, an average power flow value formed from all the rows across the beam width was assumed to be more representative than the power flow value calculated from a single row.
5. The ESPI technique was less accurate than the two-accelerometer method which employs a correction for the finite difference approximation.
6. The ESPI technique was more accurate than the simple two-accelerometer method which does not employ a correction for the finite difference approximation. However, this was only found to be true for the most favourable cases, 801 Hz and 1112 Hz, when the experimental beam best replicated “infinite” beam conditions. At the other excitation frequency, 1147 Hz, when larger amplitude reflected bending waves were present in combination with unwanted torsional motion the accuracy of the ESPI method decreased to less than that of the simple two-accelerometer technique.

Further work is now required to investigate the accuracy of the ESPI power flow technique in high standing wave environments. In principle, the ESPI power flow method can be applied under such conditions since this investigation has shown that the beam displacement can be decomposed into incident waves propagating from the source and reflected waves due to

discontinuities. However, practical issues, such as the corrupting effect of noise on the measured data, will need to be carefully addressed. An extension of the method to the near field of the vibration, close to the source of excitation or to discontinuities, would also be desirable. This would enable more wavelengths of the displacement to be recorded, hence, improving the wavenumber domain resolution. Having an advanced whole field laser measurement technique in place the extension to two-dimensional plate vibration will also be a future objective.

References

[1] D. U. Noiseux: Measurement of power flow in uniform beams and plates. Journal of the Acoustical Society of America **47** (1970) 238-247.

[2] G. Pavic: Measurement of structure borne wave intensity, Part I: formulation of the methods. Journal of Sound and Vibration **49** (1976) 221-230.

[3] CETIM: Structural Intensity and Vibrational Energy Flow. Proceedings of the Fourth International Congress on Intensity Techniques (1993).

[4] S. I. Hayek, M. J. Pechersky, B. C. Suen: Measurement and analysis of near and far field structural intensity by scanning laser vibrometry. Proceedings of the Third International Congress on Intensity Techniques (1990) 281-288.

[5] E. G. Williams, H. D. Dardy, R. G. Fink: A technique for measurement of structure-borne intensity in plates. Journal of the Acoustical Society of America **78** (1985) 2061-2068.

[6] R. J. Unglenieks, R. J. Bernhard: Measurement of flexural structural intensity using wavenumber techniques. Proceedings of the 4th International Congress on Intensity Techniques (1993) 305-311.

[7] R. Morikawa, S. Ueha, K. Nakamura: Error evaluation of the structural intensity measured with a scanning laser Doppler vibrometer and a k-space signal processing. Journal of the Acoustical Society of America **99** (1996) 2913-2921.

[8] J. D. Maynard, E. G. Williams, Y. Lee: Near field acoustical holography (NAH) 1: theory of generalised holography and the development of NAH. Journal of the Acoustical Society of America **78** (1985) 1395-1413.

[9] J. C. Pascal, X. Carniel, V. Chalvidan, P. Smigielski: Determination of phase and magnitude of vibration for energy flow measurements in a plate using holographic interferometry. Optics and Lasers in Engineering **25** (1996) 343-360.

[10] J. C. Davies, C. H. Buckberry, J. D. C. Jones C. N. Panell: Development and application of a fibre optic electronic speckle pattern interferometer. Proceeding of the SPIE **863** (1987) 194-207.

[11] J. Jones, J. Valera, C. H. Buckberry, D. P. Towers: Lasers measure up for the car industry. Physics World May (1995) 33-38.

[12] D. P. Towers, C. H. Buckberry, B. C. Stockley, M. P. Jones: Measurement of complex vibrational modes and surface form - a combined measurement system. Measurement Science Technology **6** (1995) 1242-1249.

[13] L. Cremer, M. Heckl, E. E. Ungar: Structure-Borne Sound: Structural vibration and sound radiation at audio frequencies. Springer Verlag, Berlin, 1988, 2nd edition.

[14] Y. Zhang, J. A. Mann III: Measuring the structural intensity and force distribution in plates. Journal of the Acoustical Society of America **99** (1996) 345-353.

[15] A. Nejade, R. Singh: Flexural intensity measurements on finite plates using modal spectrum ideal filtering. Journal of Sound and Vibration **256** (2002) 33-63.

[16] H. G. D. Goyder, R. G. White: Vibrational power flow from machines into built-up structures. Part I: Introduction and approximate analyses of beam and plate-like foundations. Journal of Sound and Vibration **68** (1980) 59-75.

[17] J. W. Verheij: Cross spectral density methods for measuring structure borne power flow in beams and pipes. Journal of Sound and Vibration **70** (1980) 133-139.

[18] W. Redman-White: The experimental measurement of flexural wave power in structures. Proceedings of the Second International Conference on Recent Advances in Structural Dynamics (1984) 467-474.

[19] J. Linjama, T. Lahti: Measurement of bending wave reflection and impedance in a beam by the structural intensity technique. Journal of Sound and Vibration **161** (1993) 317-331.

Figure 1.
First author: Eck.

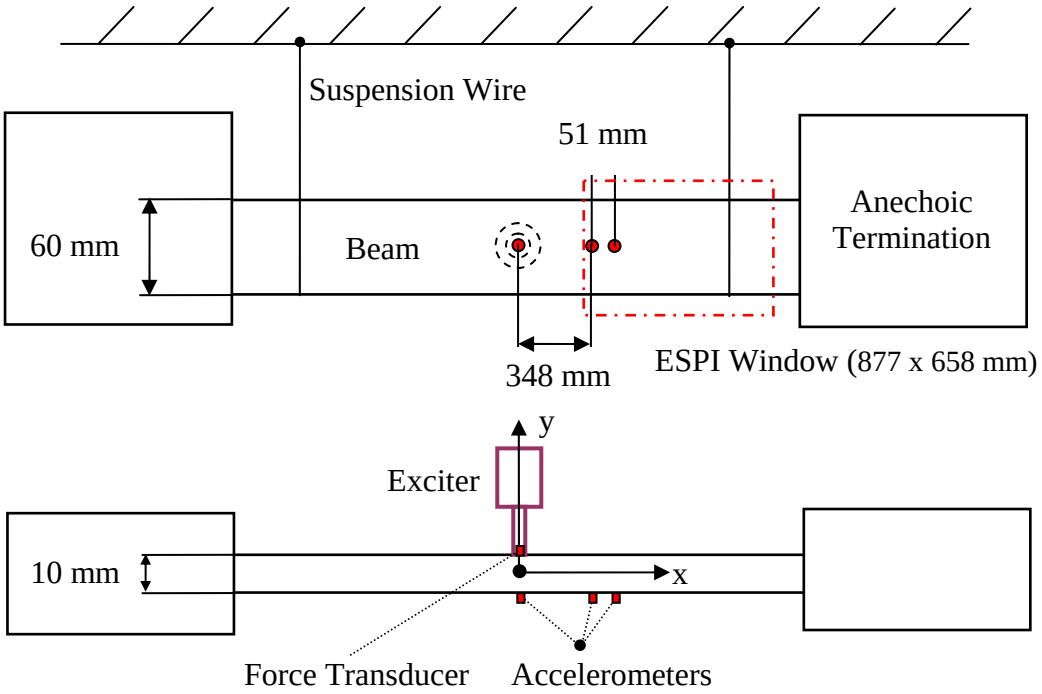

Figure 1. Experimental “infinite” beam apparatus.

Figure 2.
First author: Eck.

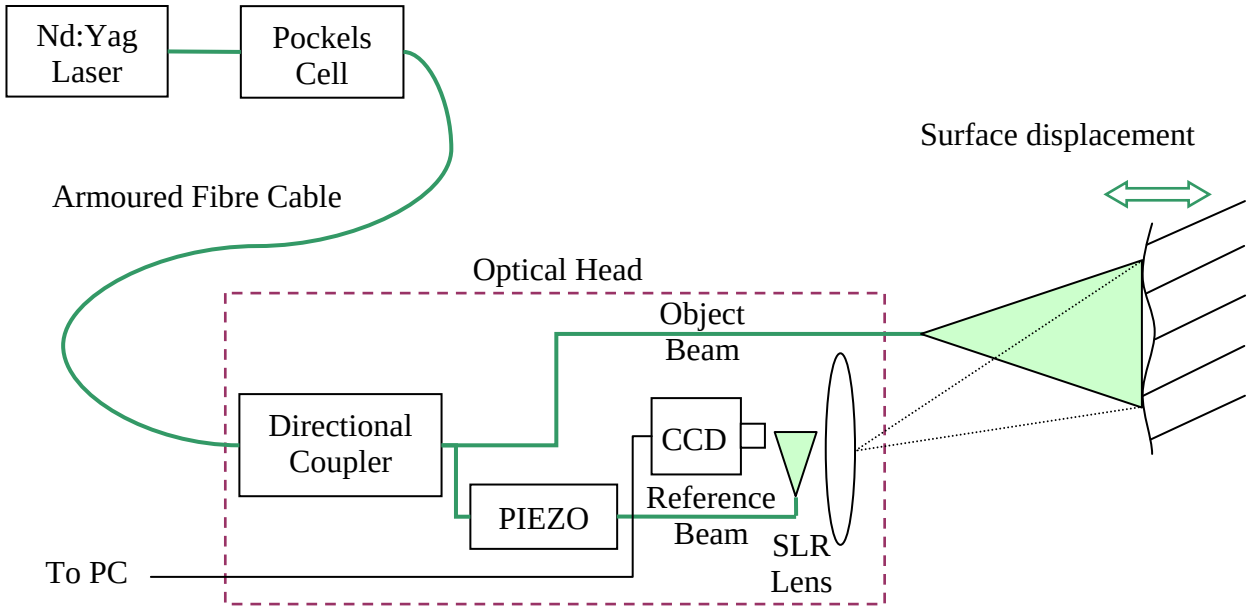

Figure 2. ESPI measurement system.

Figure 3.
First author: Eck.

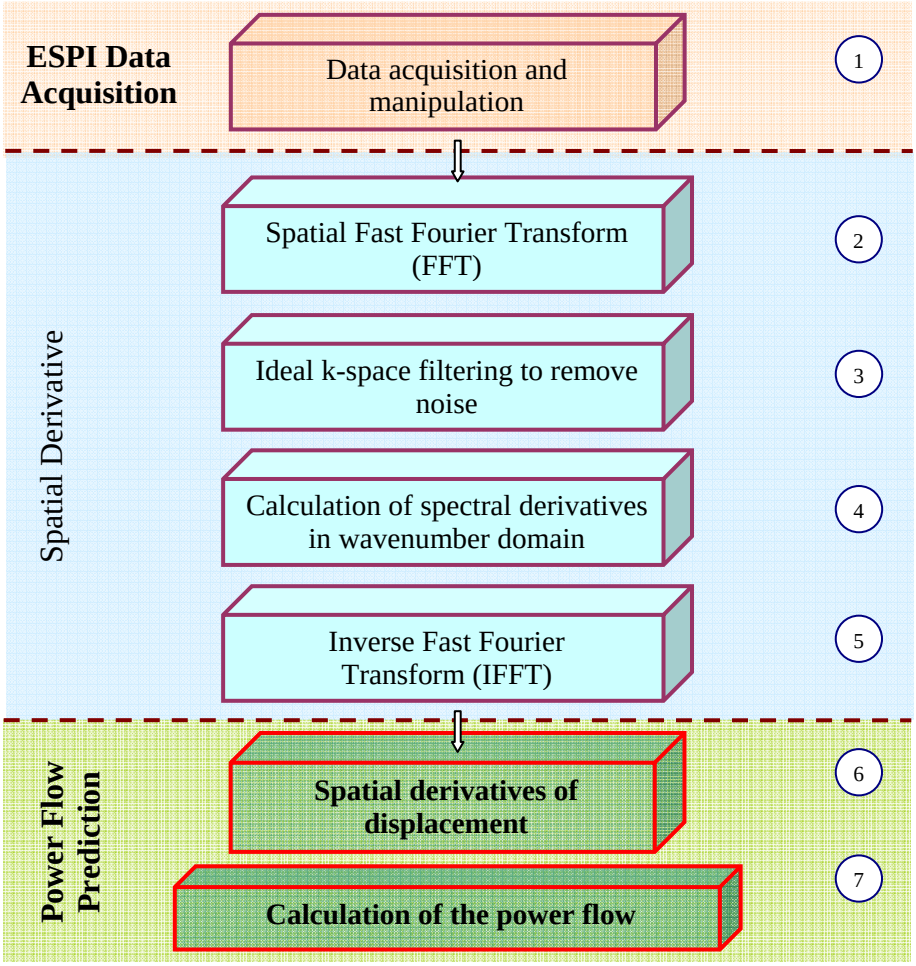

Figure 3. Flow diagram of power flow calculation.

Figure 4.
First author: Eck.

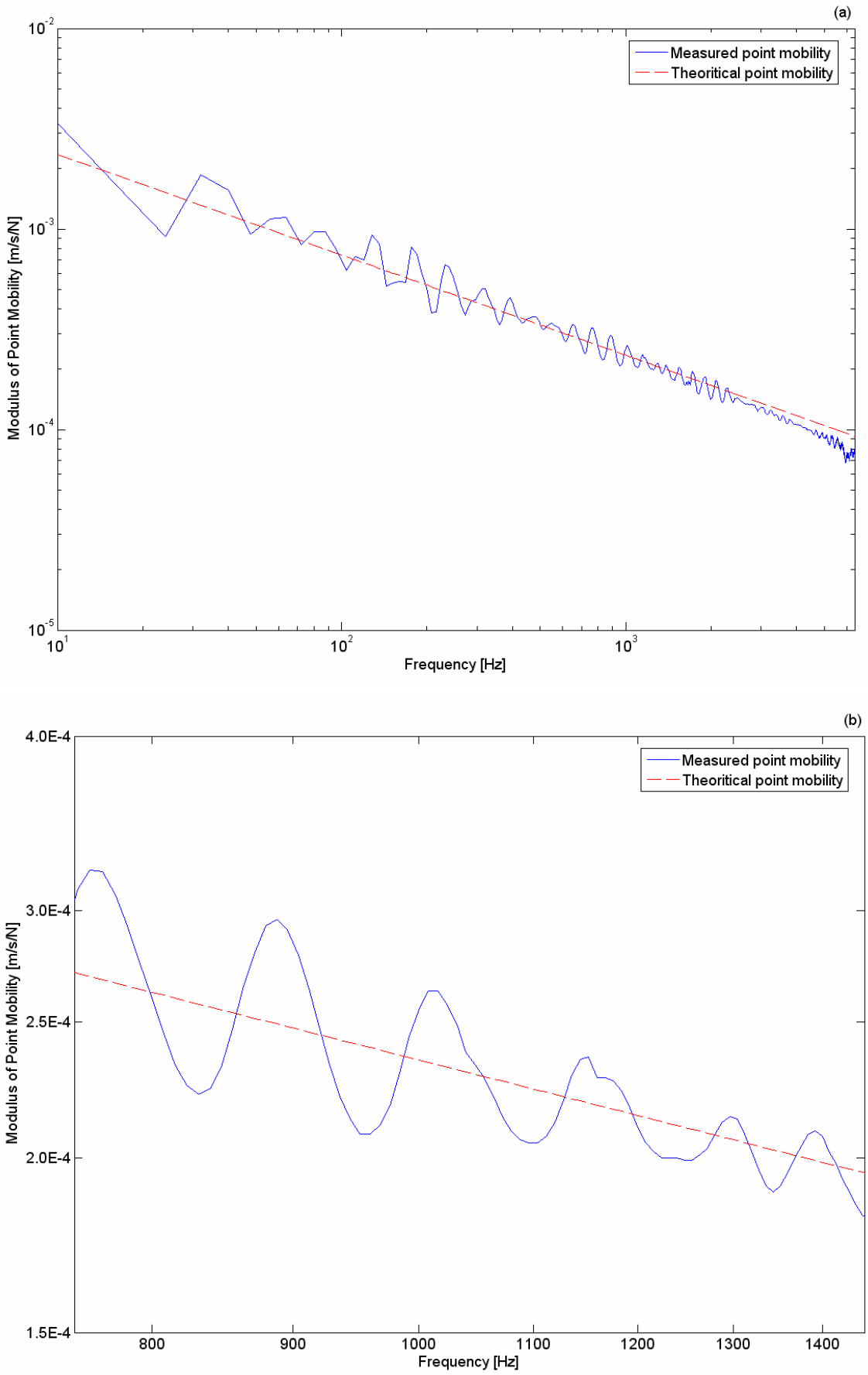

Figure 4. Driving Point mobility of the experimental "infinite" beam, measured (——) and theoretical (-----), (a) 10-10kHz, (b) 750-1450 Hz.

Figure 5.
First author: Eck.

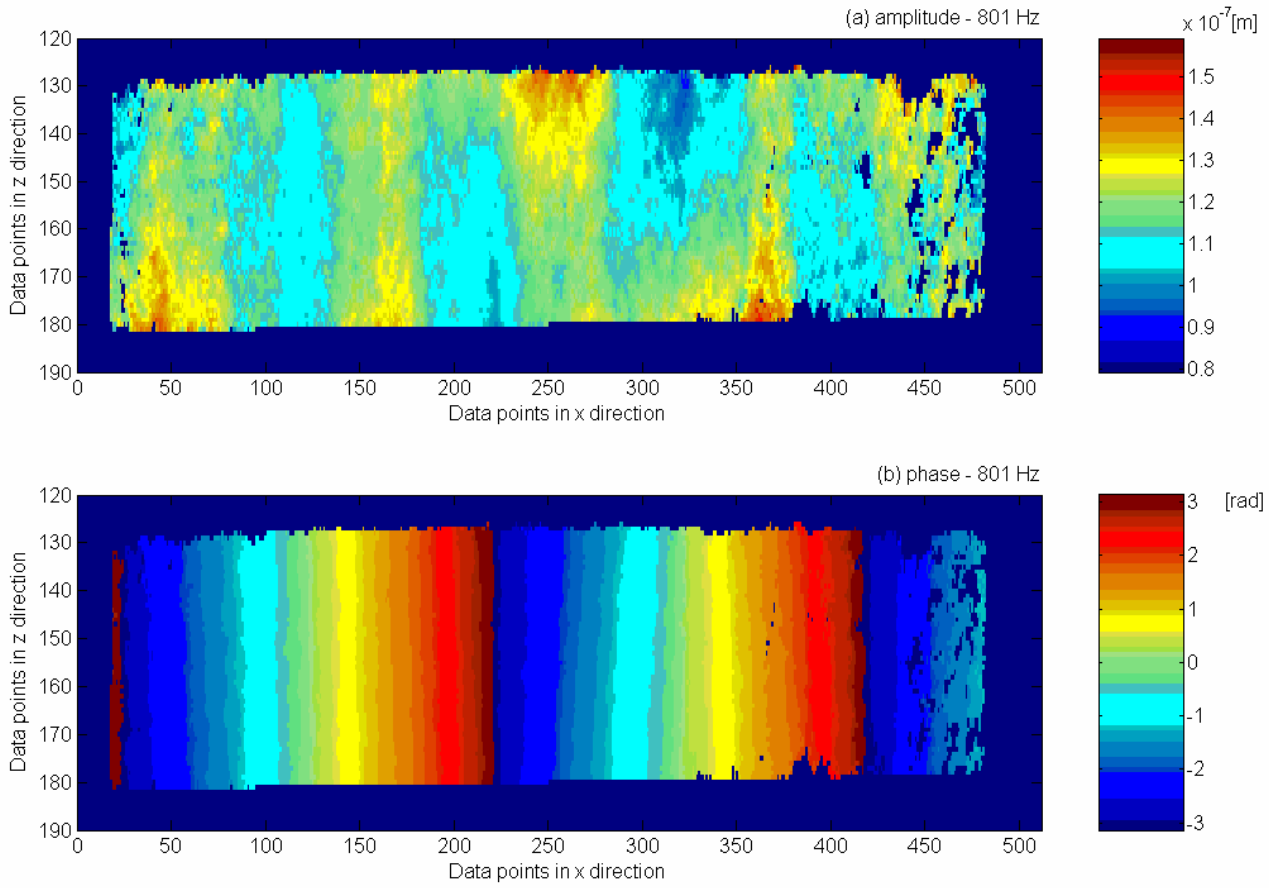

Figure 5. ESPI image of beam displacement excited by a harmonic force at 801 Hz, (a) amplitude, (b) phase.

Figure 6.
First author: Eck.

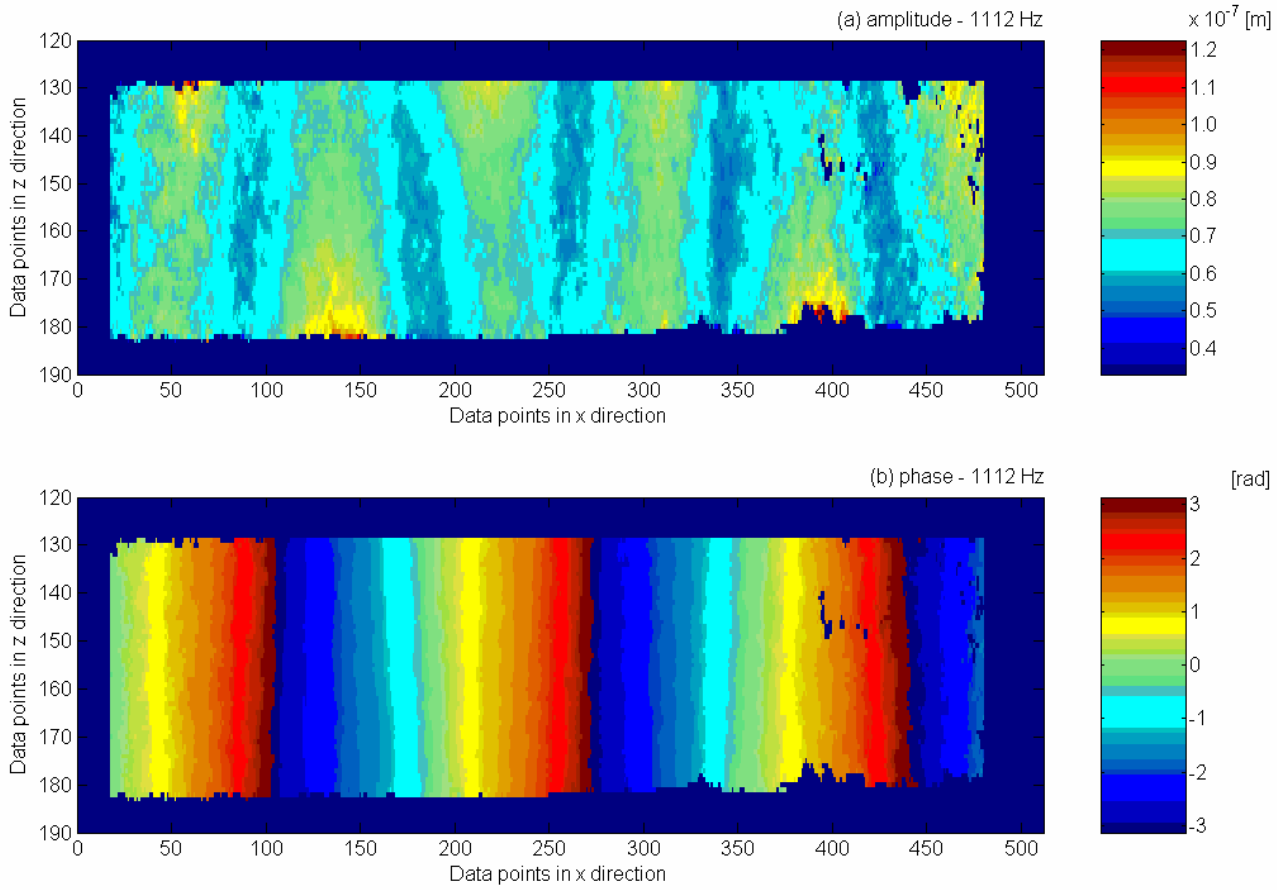

Figure 6. ESPI image of beam displacement excited by a harmonic force at 1112 Hz, (a) amplitude, (b) phase.

Figure 7.
First author: Eck.

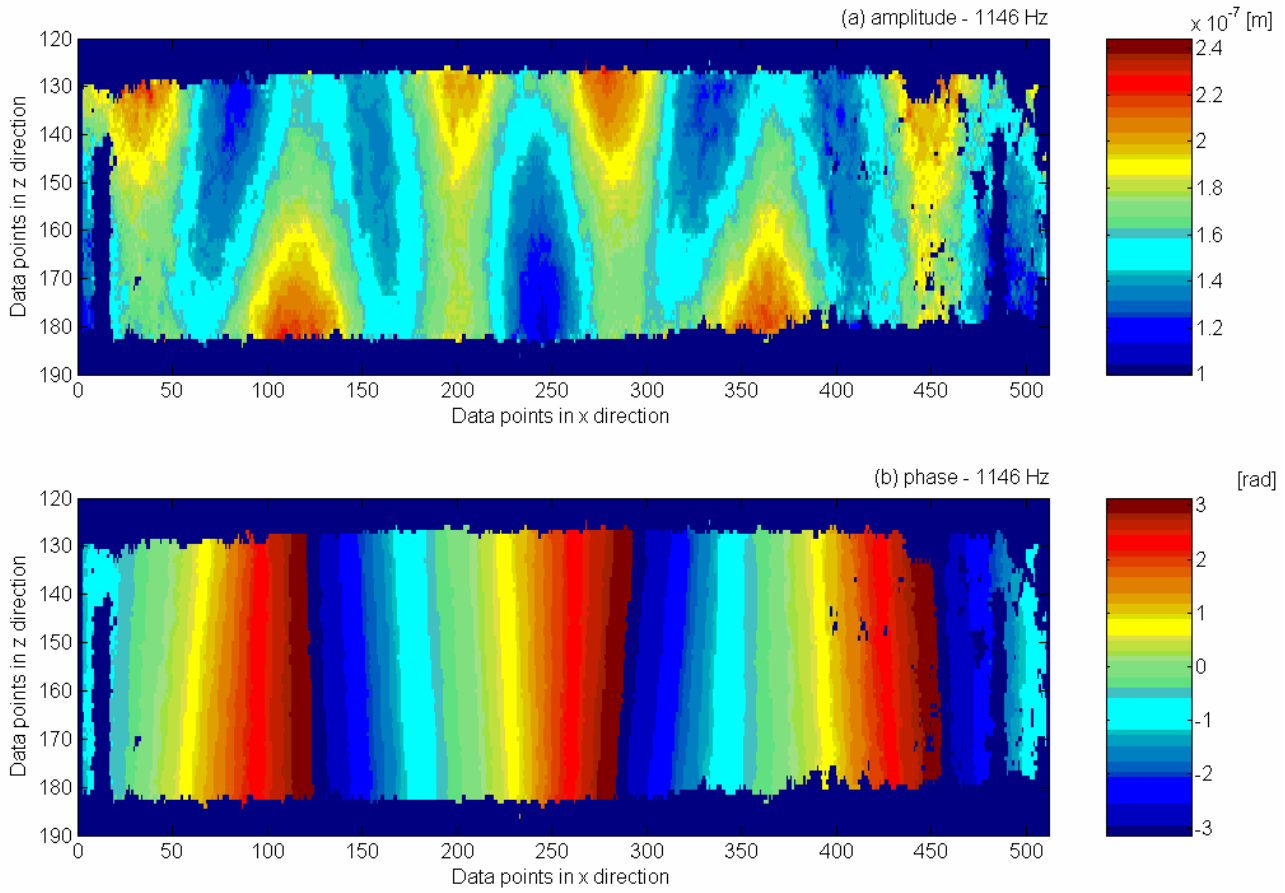

Figure 7. ESPI image of beam displacement excited by a harmonic force at 1146 Hz, (a) amplitude, (b) phase.

Figure 8.
First author: Eck.

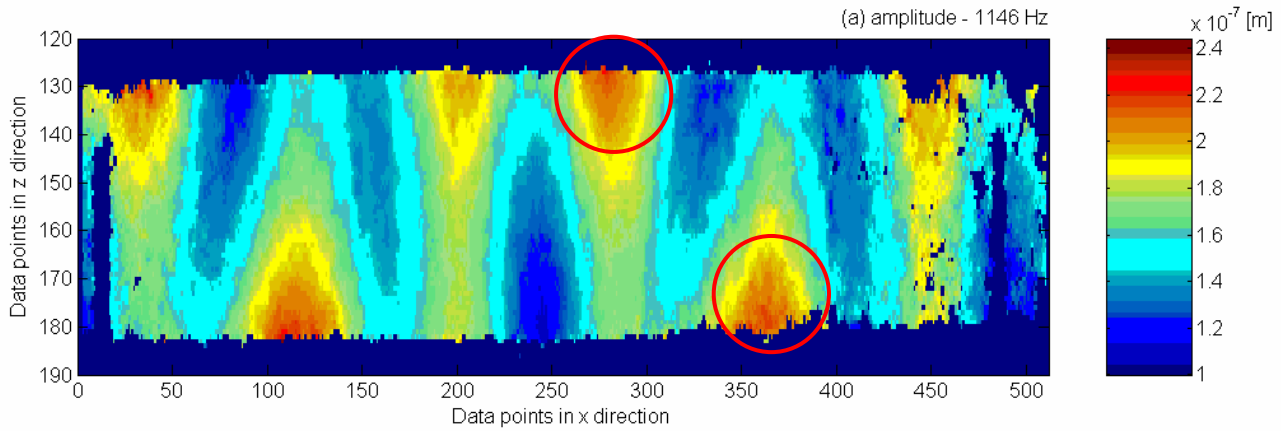

Figure 8. Beam displacement amplitude showing regions of high vibration amplitude due to torsional vibration at 1146 Hz (indicated with circles).

Figure 9.
First author: Eck.

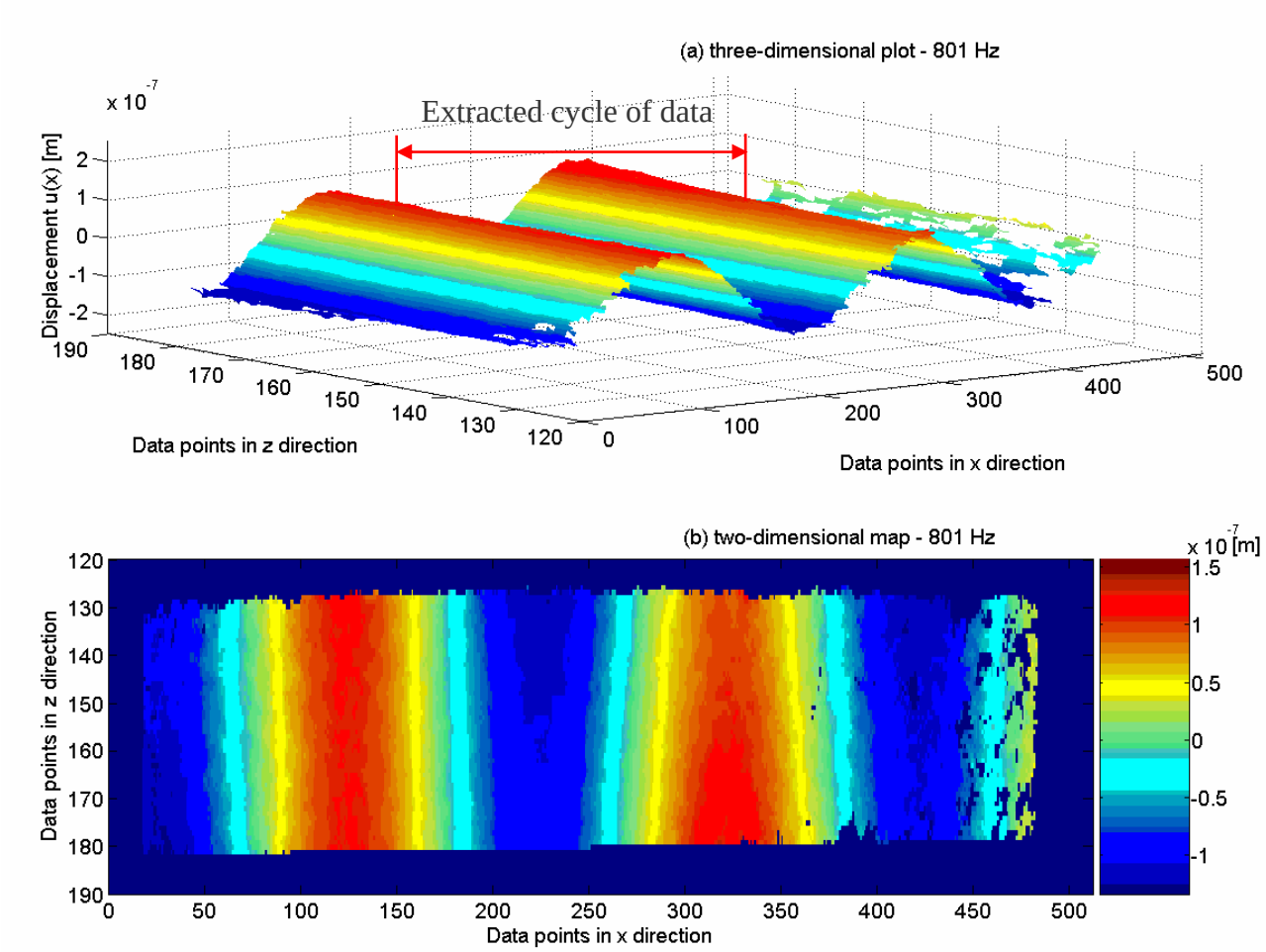

Figure 9. Real part of the beam displacement at 801 Hz showing the single cycle extracted for wavenumber transformation: (a) three-dimensional plot, (b) two-dimensional map.

Figure 10.
First author: Eck.

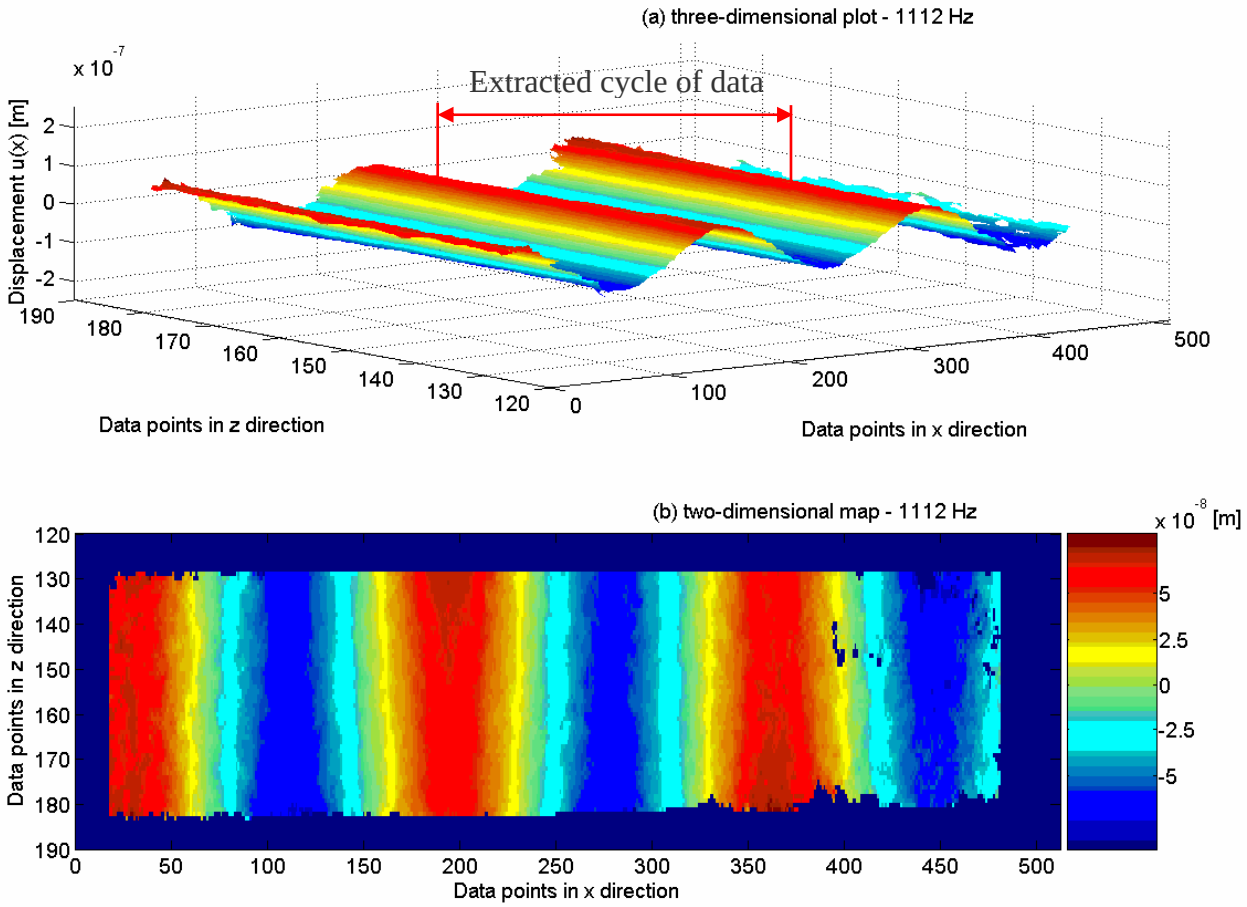

Figure 10. Real part of the beam displacement at 1112 Hz showing the single cycle extracted for wavenumber transformation: (a) three-dimensional plot, (b) two-dimensional map.

Figure 11.
First author: Eck.

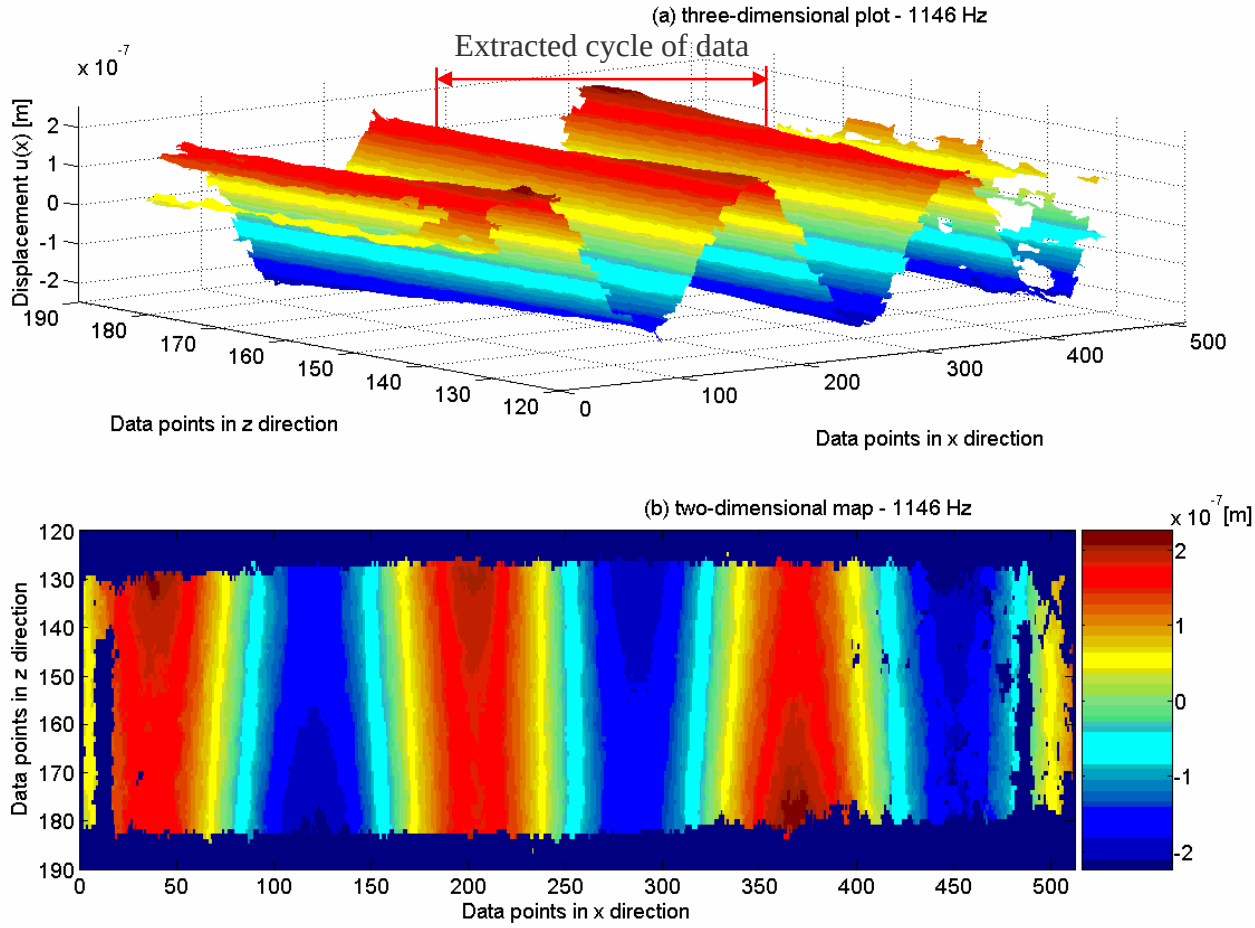

Figure 11. Real part of the beam displacement at 1146 Hz showing the single cycle extracted for wavenumber transformation: (a) three-dimensional plot, (b) two-dimensional map.

Figure 12.
First author: Eck.

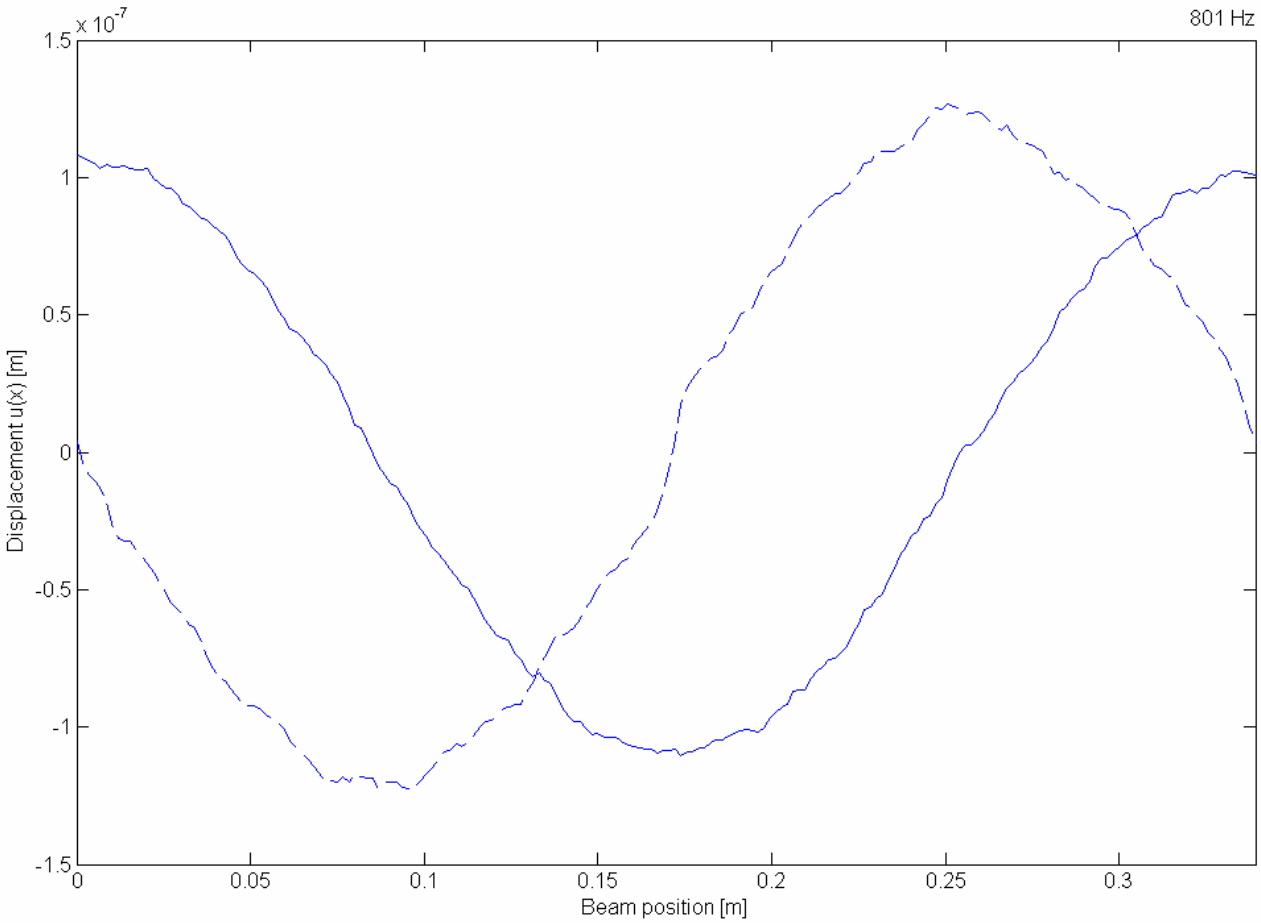

Figure 12. Real part (——) and imaginary part (----) of row 150 from a single cycle of beam displacement at 801 Hz.

Figure 13.
First author: Eck.

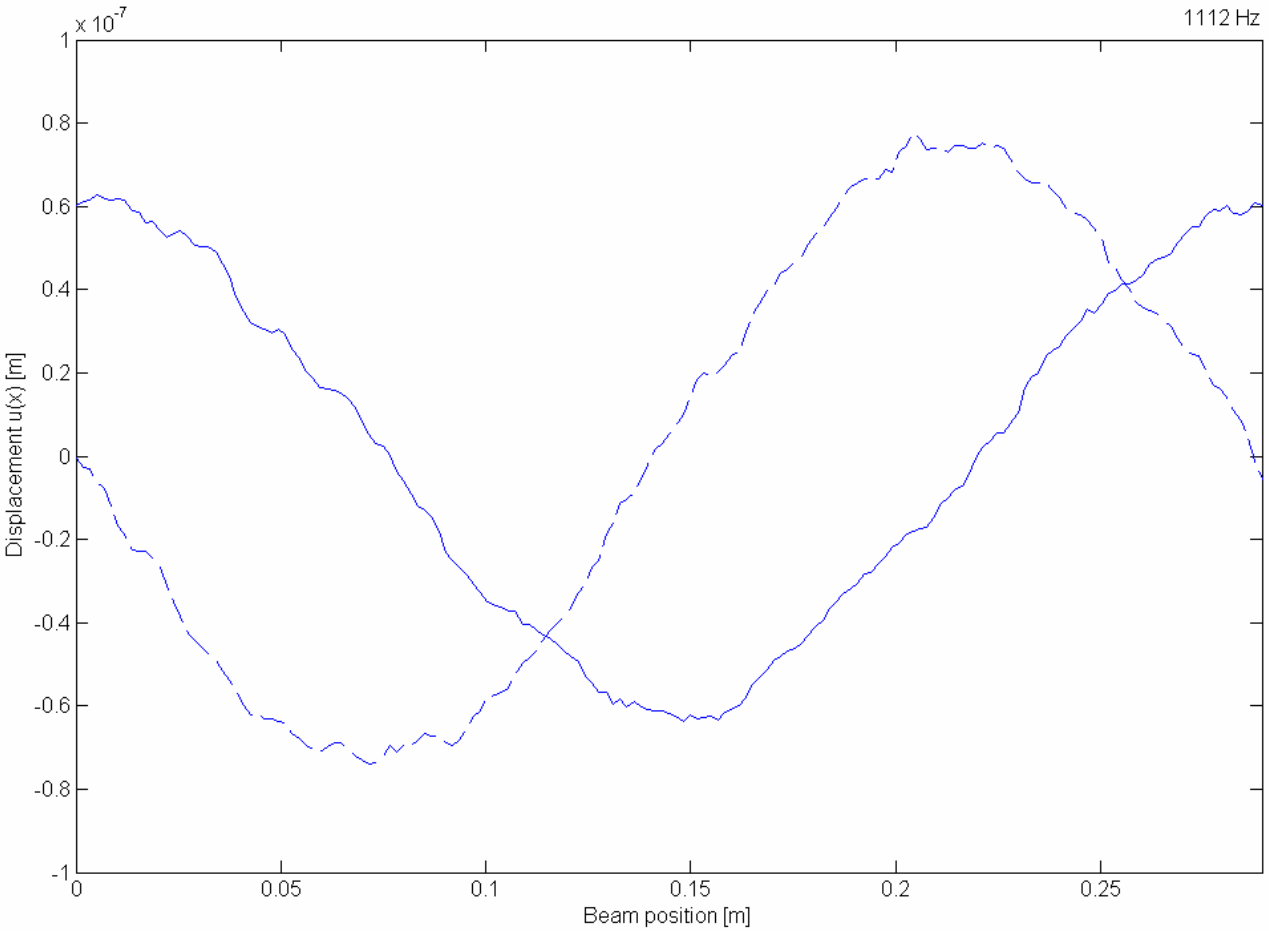

Figure 13. Real part (——) and imaginary part (----) of row 150 from a single cycle of beam displacement at 1112 Hz.

Figure 14.
First author: Eck.

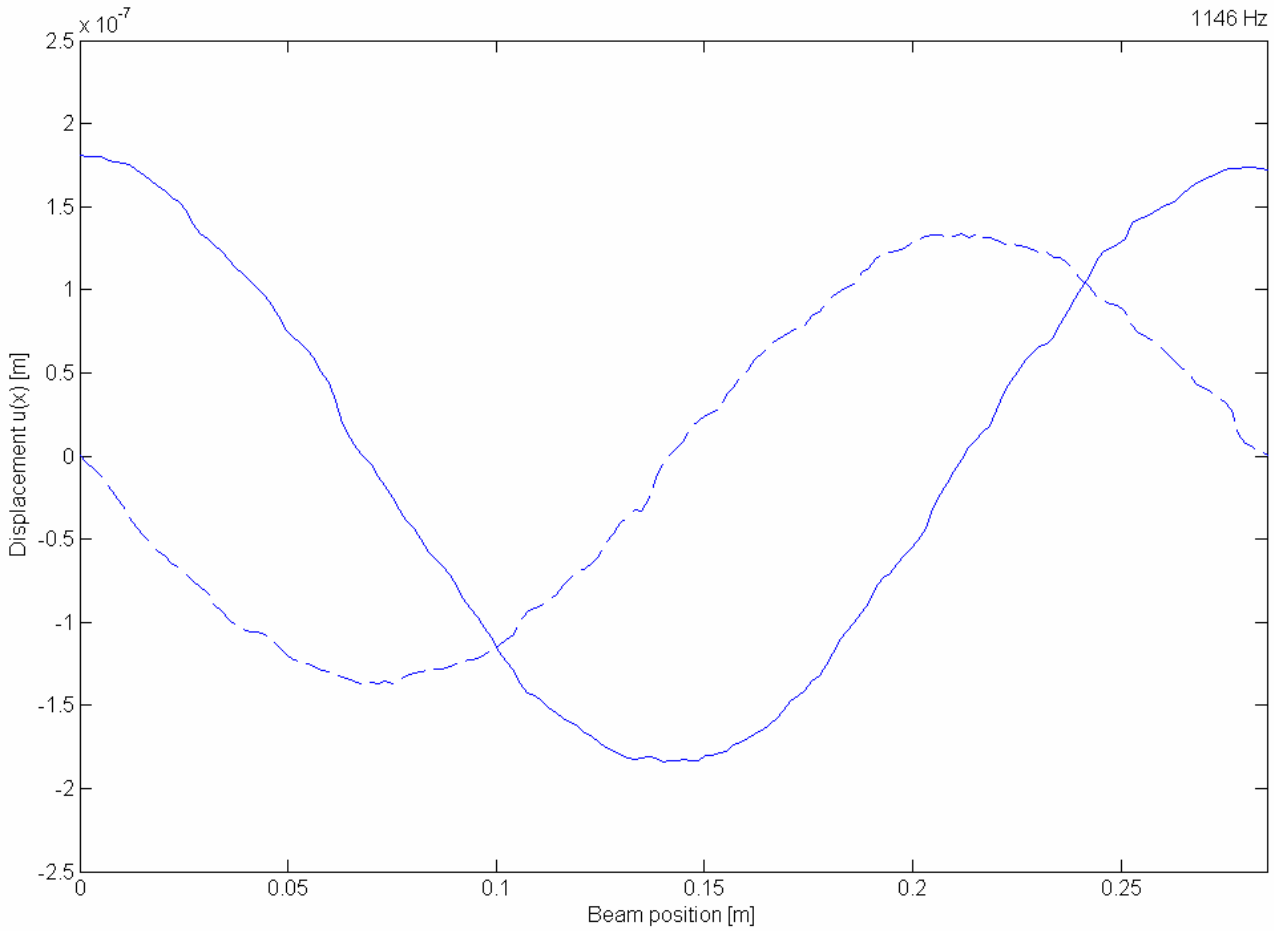

Figure 14. Real part (——) and imaginary part (----) of row 150 from a single cycle of beam displacement at 1146 Hz.

Figure 15.
First author: Eck.

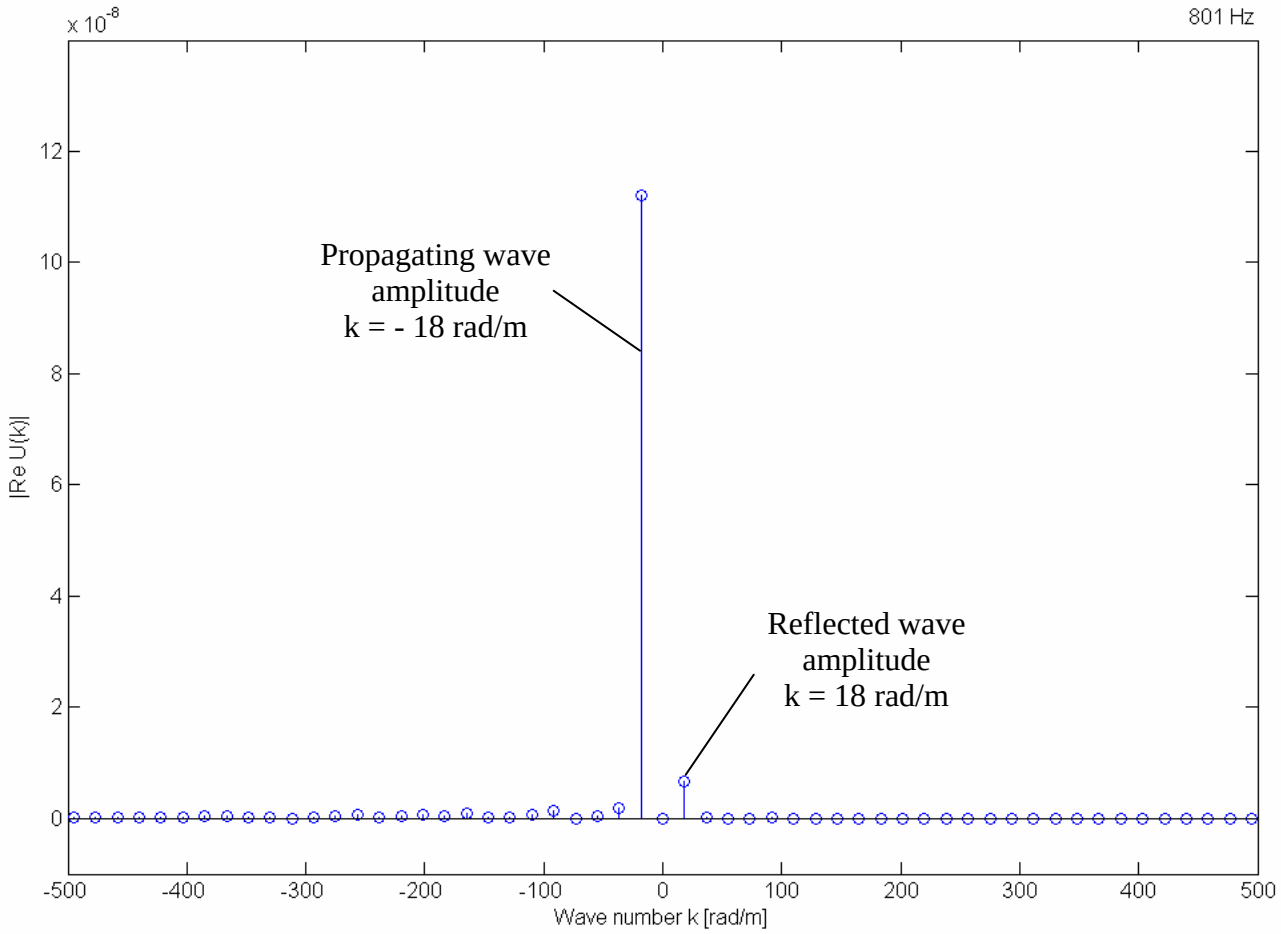

Figure 15. Real part of the wavenumber spectrum of the displacement showing propagating and reflected wave components at 801 Hz.

Figure 16.
First author: Eck.

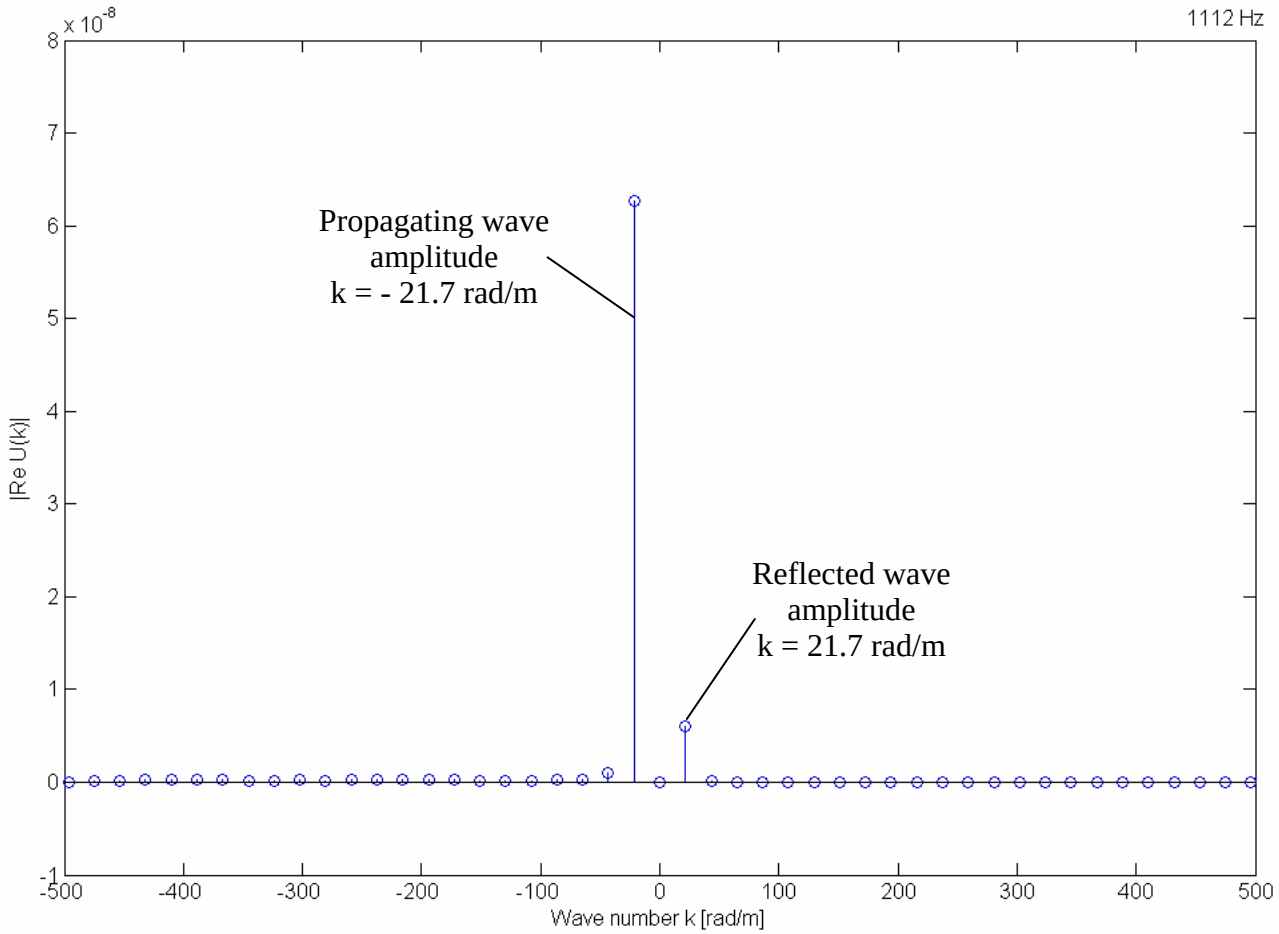

Figure 16. Real part of the wavenumber spectrum of the displacement showing propagating and reflected wave components at 1112 Hz.

Figure 17.
First author: Eck.

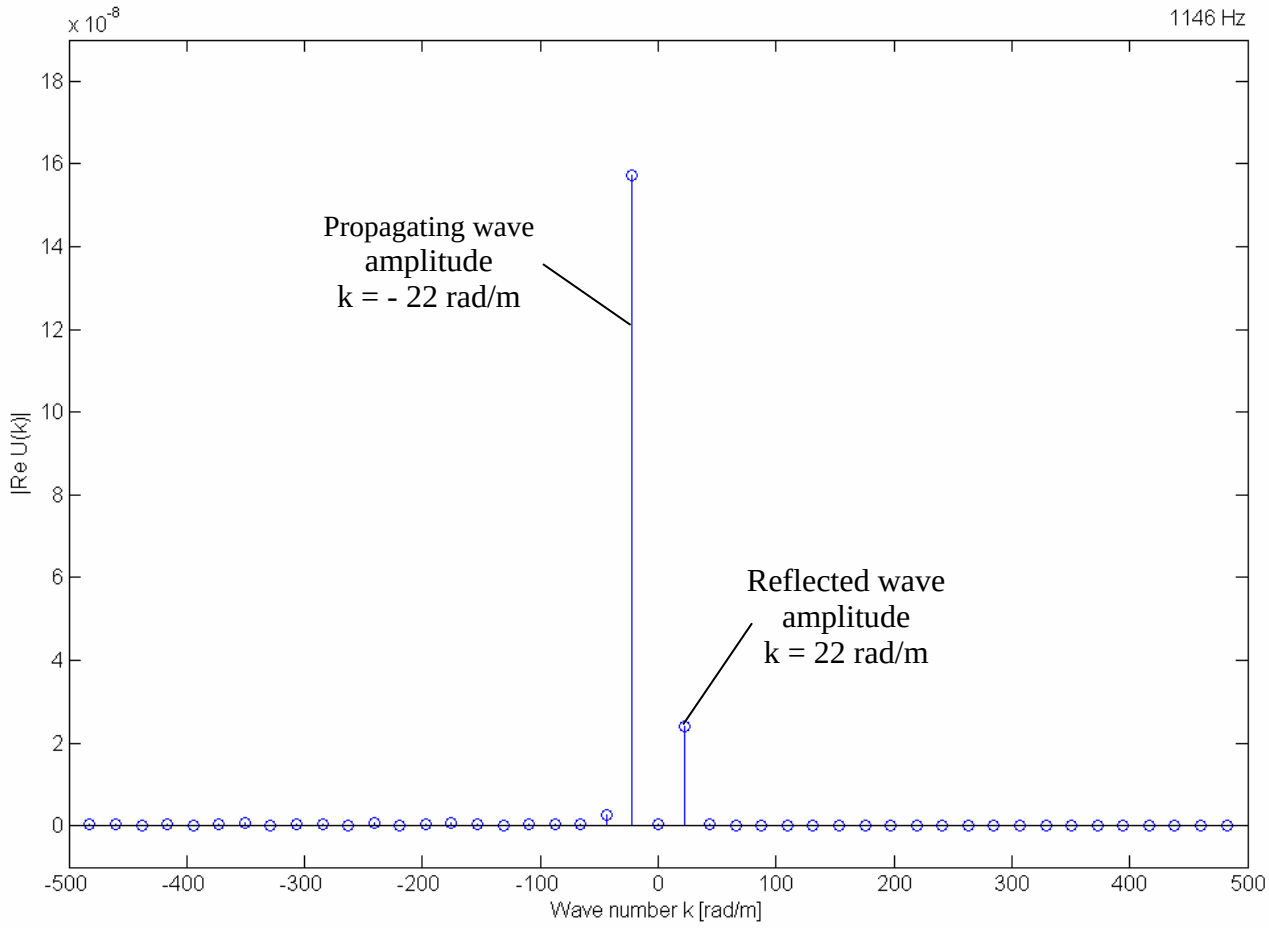

Figure 17. Real part of the wavenumber spectrum of the displacement showing propagating and reflected wave components at 1147 Hz.

Figure 18.
First author: Eck.

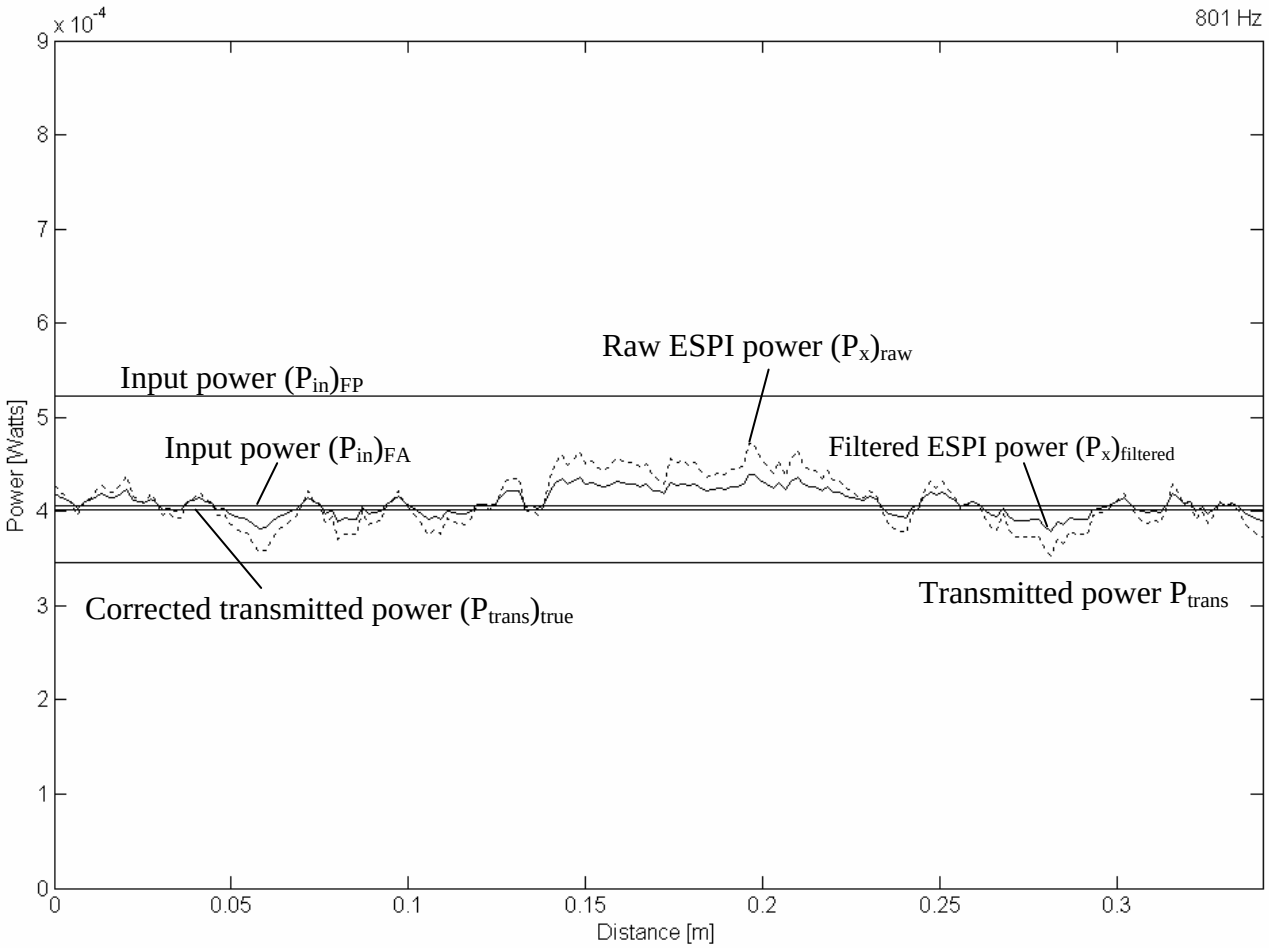

Figure 18. Comparison of measured input power and measured transmitted power against distance along the ESPI window of the experimental beam at 801 Hz, row 150.

Figure 19.
First author: Eck.

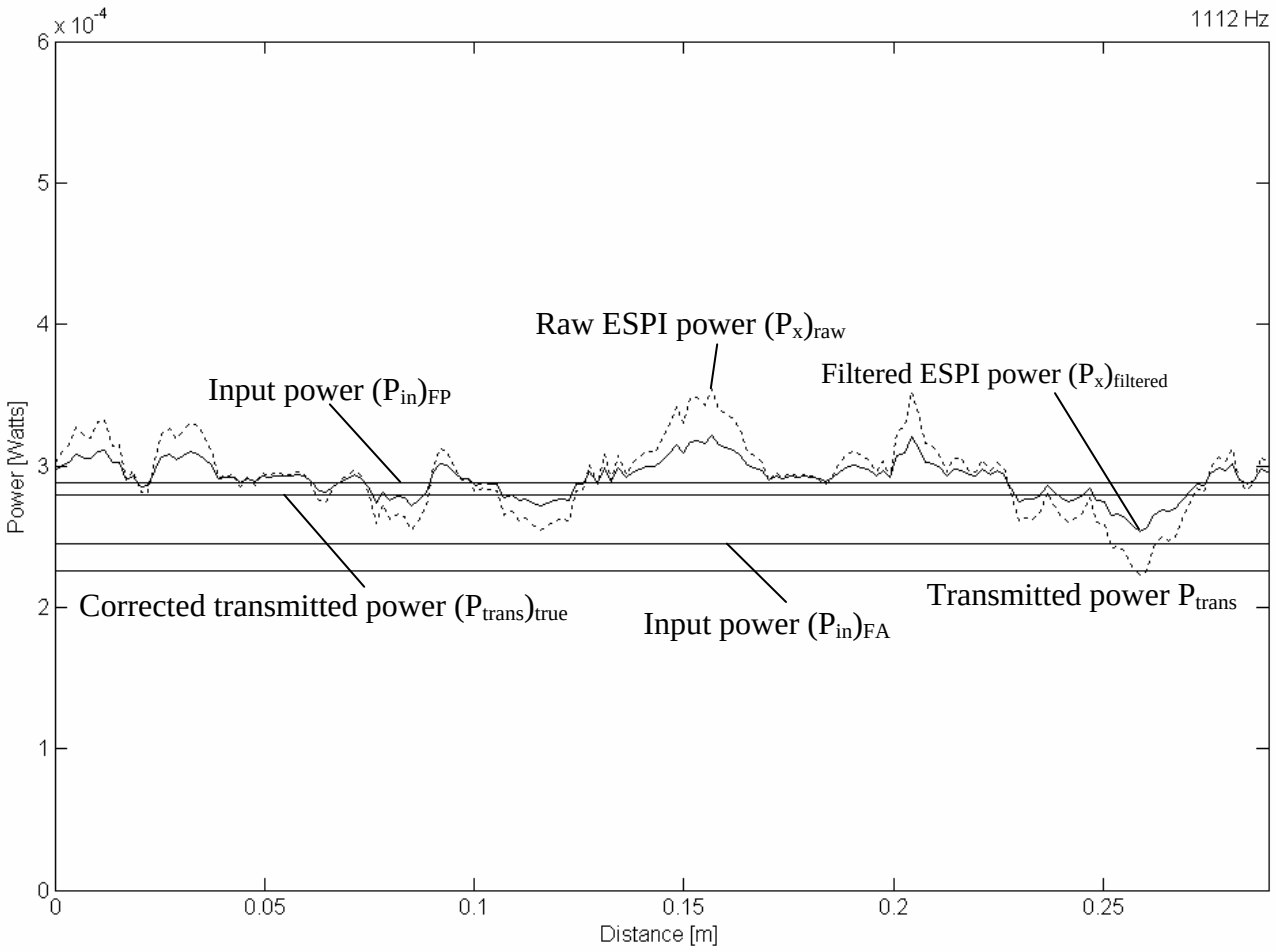

Figure 19. Comparison of measured input power and measured transmitted power against distance along the ESPI window of the experimental beam at 1112 Hz, row 150.

Figure 20.
First author: Eck.

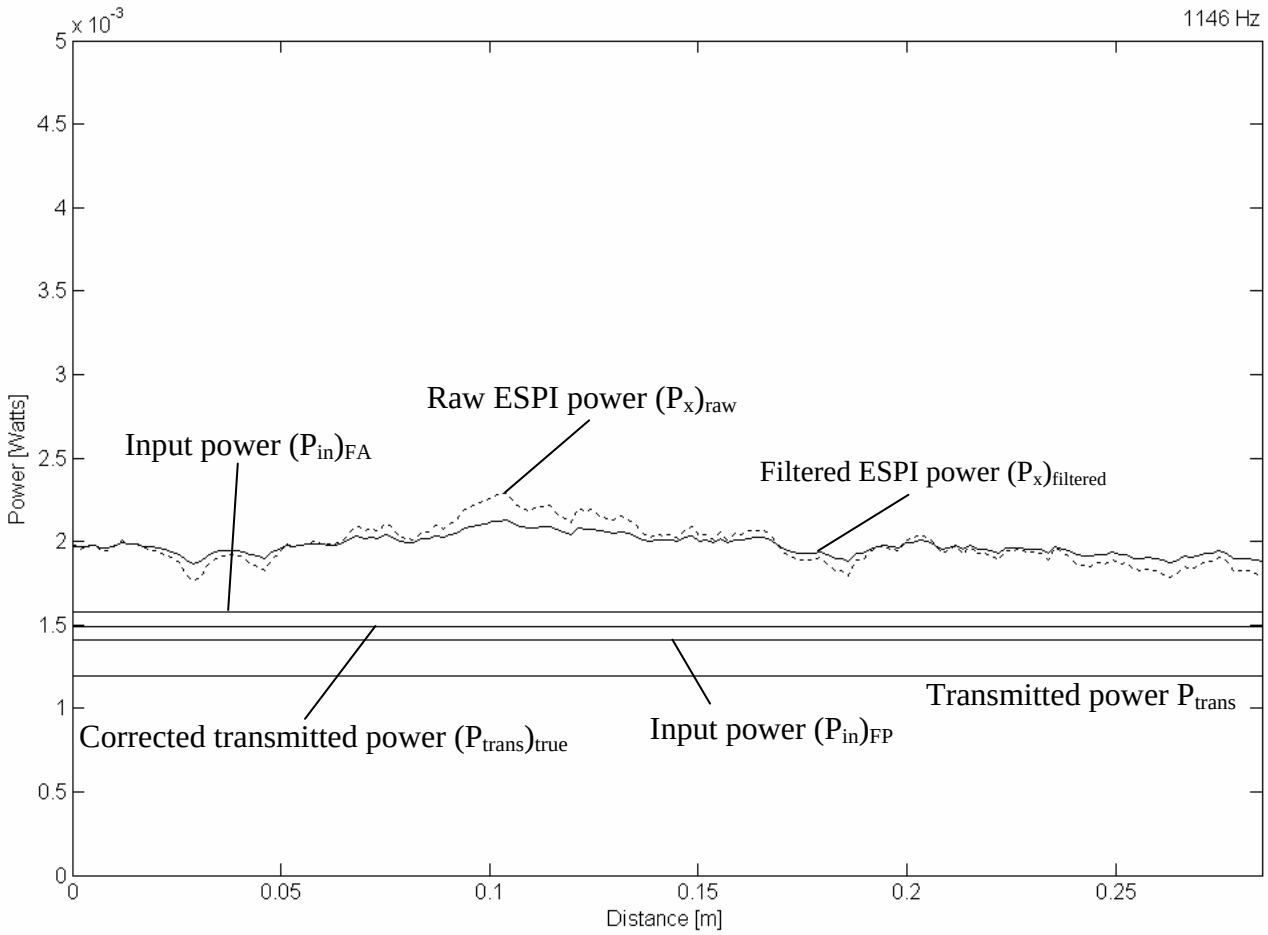

Figure 20. Comparison of measured input power and measured transmitted power against distance along the ESPI window of the experimental beam at 1146 Hz, row 150.

Figure 21.
First author: Eck.

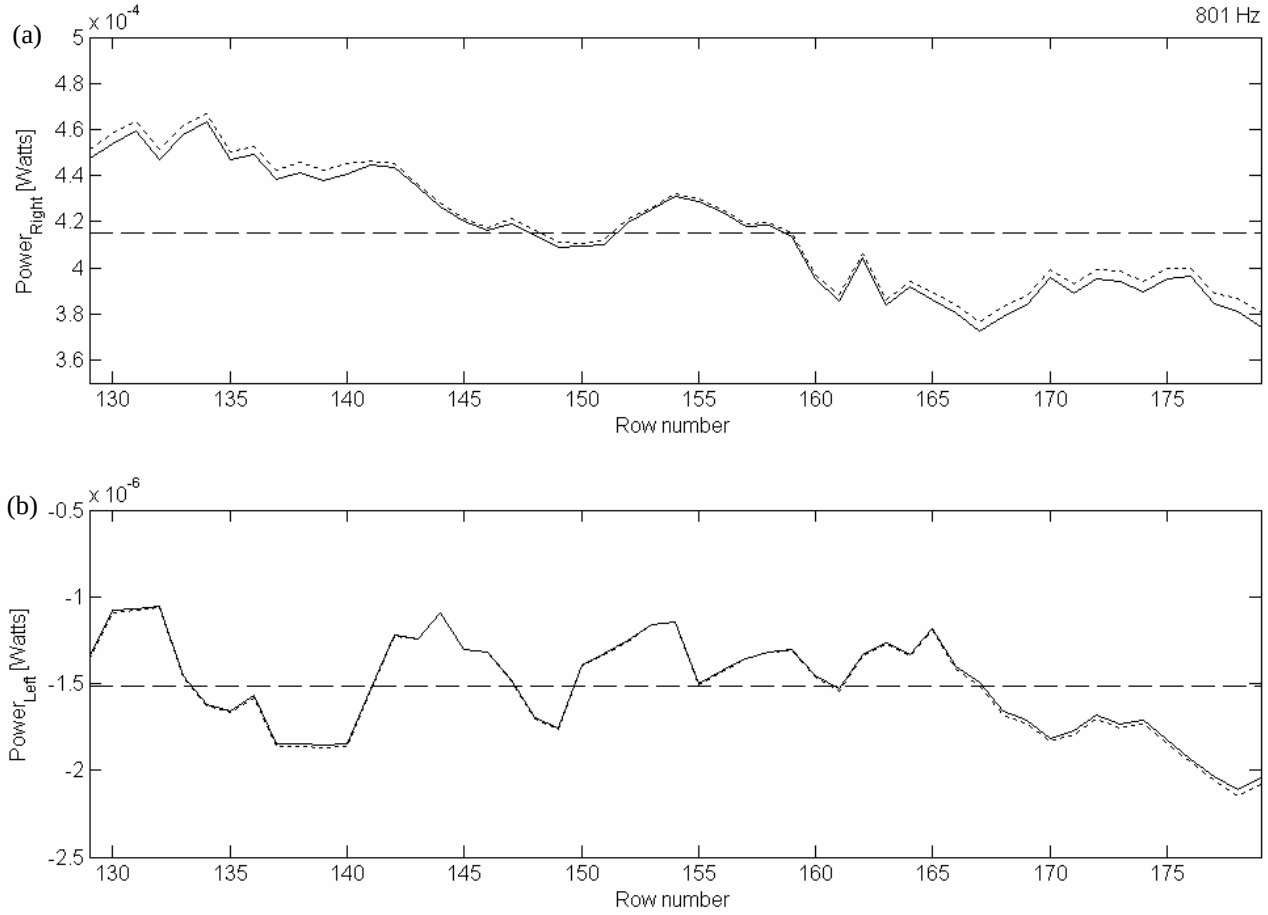

Figure 21. Power flow distribution across the beam width, raw ESPI power (·····), filtered ESPI power (——) and averaged value (----) at 801 Hz: (a) right going wave; (b) left going wave.

Figure 22.
First author: Eck.

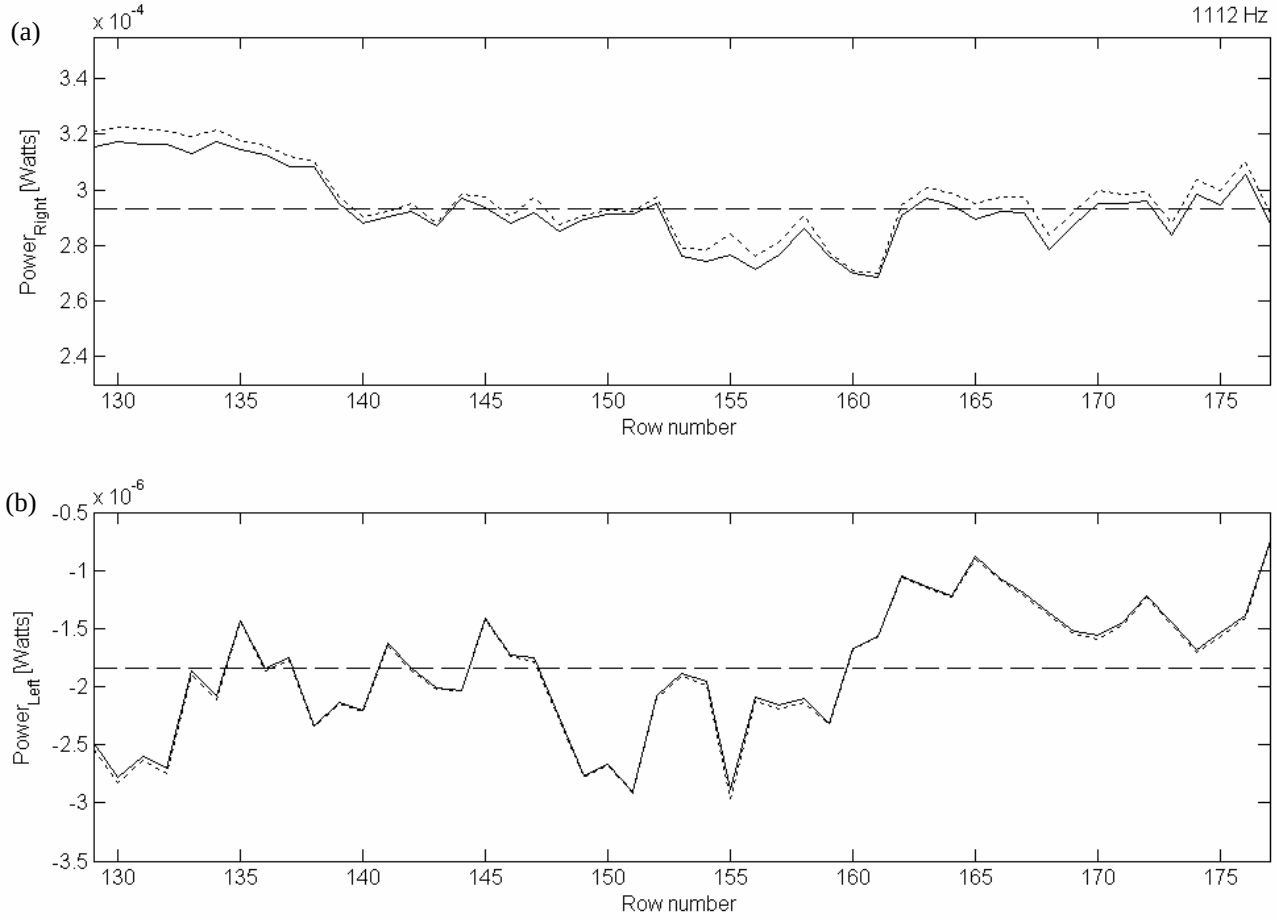

Figure 22. Power flow distribution across the beam width, raw ESPI power (·····), filtered ESPI power (——) and averaged value (----) at 1112 Hz: (a) right going wave; (b) left going wave.

Figure 23.
First author: Eck.

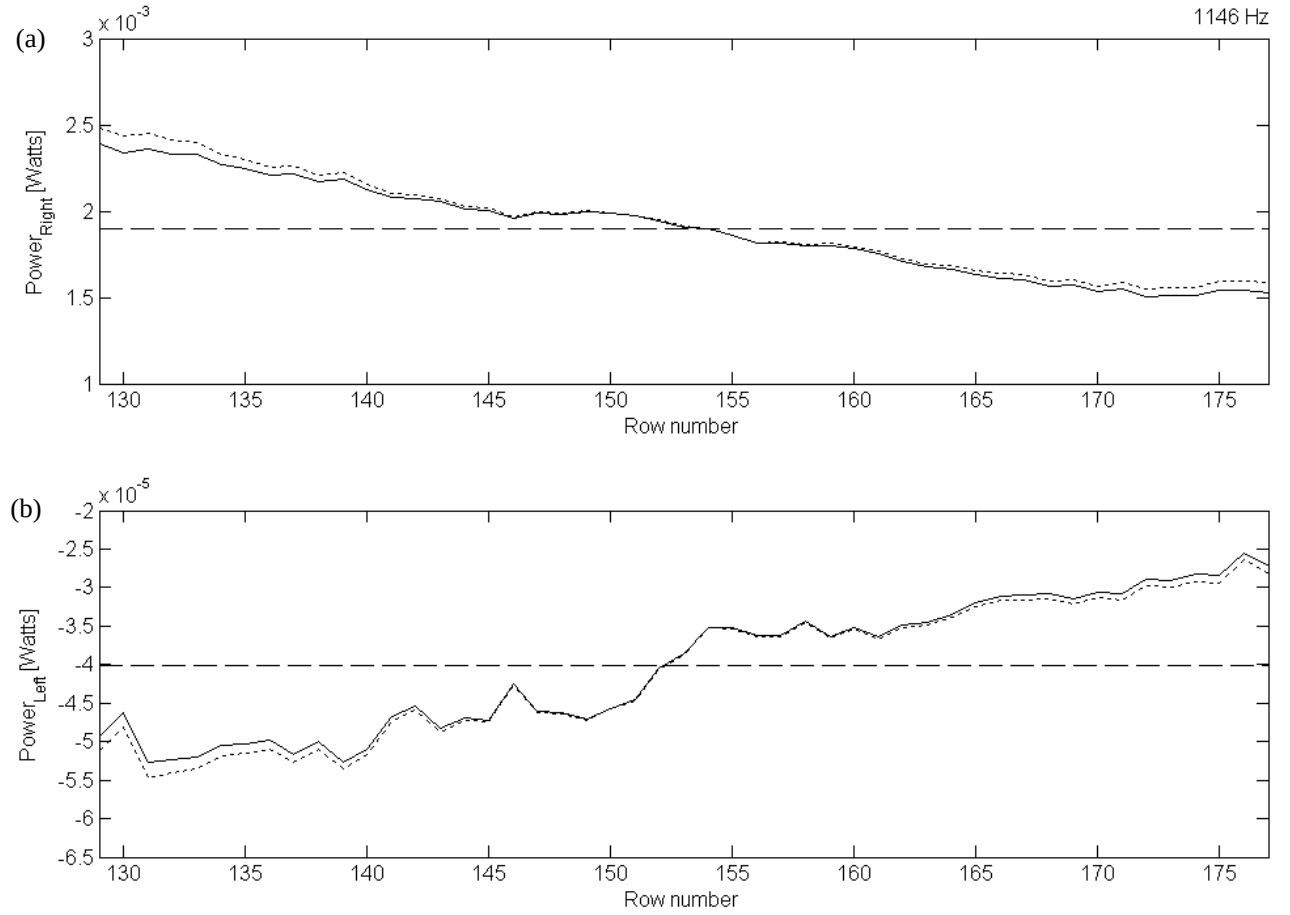

Figure 23. Power flow distribution across the beam width, raw ESPI power (·····), filtered ESPI power (——) and averaged value (----) at 1146 Hz: (a) right going wave; (b) left going wave.

	801 Hz	1112 Hz	1146 Hz
Wave amplitudes			
Right going wave, $\|A_i\|$ [m]	$1.140 \cdot 10^{-7}$	$6.588 \cdot 10^{-8}$	$1.567 \cdot 10^{-7}$
Left going wave, $\|A_r\|$ [m]	$8.994 \cdot 10^{-9}$	$7.473 \cdot 10^{-9}$	$2.184 \cdot 10^{-8}$
Reflection coefficients			
ESPI measurements, $\|R_1\|$	0.0789	0.1134	0.1394
Two-accelerometer measurements, $\|R_2\|$	0.0896	0.1255	0.1239

Table 1. Wave amplitudes and reflection coefficients.

Power quantity	801 Hz [Watts]	1112 Hz [Watts]	1146 Hz [Watts]
Input power measurements			
Half input power, $(P_{in})_{FP}$	$5.23 \cdot 10^{-4}$	$2.88 \cdot 10^{-4}$	$1.41 \cdot 10^{-3}$
Half input power, $(P_{in})_{FA}$	$4.04 \cdot 10^{-4}$	$2.45 \cdot 10^{-4}$	$1.58 \cdot 10^{-3}$
Two-accelerometer measurements			
Transmitted power, P_{trans}	$3.46 \cdot 10^{-4}$	$2.26 \cdot 10^{-4}$	$1.20 \cdot 10^{-3}$
Corrected transmitted power, $(P_{trans})_{true}$	$4.03 \cdot 10^{-4}$	$2.80 \cdot 10^{-4}$	$1.49 \cdot 10^{-3}$
ESPI measurements, single row analysis			
Raw ESPI power right, $(P_x)_{raw}$	$4.11 \cdot 10^{-4}$	$2.93 \cdot 10^{-4}$	$1.99 \cdot 10^{-3}$
Filtered ESPI power right, $(P_x)_{filtered}$	$4.09 \cdot 10^{-4}$	$2.91 \cdot 10^{-4}$	$1.98 \cdot 10^{-3}$
Raw ESPI power left, $(P_x)_{raw}$	$-1.40 \cdot 10^{-6}$	$-2.68 \cdot 10^{-6}$	$-4.65 \cdot 10^{-5}$
Filtered ESPI power left, $(P_x)_{filtered}$	$-\cdot 1.39 \cdot 10^{-6}$	$-2.67 \cdot 10^{-6}$	$-4.63 \cdot 10^{-5}$
Raw ESPI net power, $(P_x)_{raw\text{-}net}$	$4.09 \cdot 10^{-4}$	$2.90 \cdot 10^{-4}$	$1.93 \cdot 10^{-3}$
Filtered ESPI net power, $(P_x)_{filtered\text{-}net}$	$4.08 \cdot 10^{-4}$	$2.89 \cdot 10^{-4}$	$1.93 \cdot 10^{-3}$
ESPI measurements, multi-row analysis			
Raw ESPI power right, $(P_x)_{raw\text{-}multi}$	$4.18 \cdot 10^{-4}$	$2.97 \cdot 10^{-4}$	$1.93 \cdot 10^{-3}$
Filtered ESPI power right, $(P_x)_{filtered\text{-}multi}$	$4.15 \cdot 10^{-4}$	$2.93 \cdot 10^{-4}$	$1.89 \cdot 10^{-3}$
Raw ESPI power left, $(P_x)_{raw\text{-}multi}$	$-1.52 \cdot 10^{-6}$	$-1.87 \cdot 10^{-6}$	$-4.08 \cdot 10^{-5}$
Filtered ESPI power left, $(P_x)_{filtered\text{-}multi}$	$-1.51 \cdot 10^{-6}$	$-1.85 \cdot 10^{-6}$	$-4.02 \cdot 10^{-5}$
Raw ESPI net power, $(P_x)_{raw\text{-}net\text{-}multi}$	$4.16 \cdot 10^{-4}$	$2.95 \cdot 10^{-4}$	$1.89 \cdot 10^{-3}$
Filtered ESPI net power, $(P_x)_{filtered\text{-}net\text{-}multi}$	$4.13 \cdot 10^{-4}$	$2.91 \cdot 10^{-4}$	$1.86 \cdot 10^{-3}$

Table 2. Input power and transmitted power values.